SCATTERING MODEL FOR A LEAF AT MILLIMETER WAVELENGTHS

K. Sarabandi, F.T. Ulaby, and T.B.A. Senior

Radiation Laboratory, Electrical Engineering and Computer Science Department,

University of Michigan, Ann Arbor

Abstract

At millimeter wave frequencies a typical leaf is a significant fraction of a wavelength in thickness, and its nonuniform dielectric profile now affects the scattering. To provide a simple and efficient method for predicting the scattering, two types of physical optics approximations are examined. The first approximates the volume polarization current by the current which would exist in an infinite dielectric slab with the same profile, while the second (and simpler) one employs the surface current which, on the infinite slab, produces the known reflected field. It is shown that the first method is superior, and provided the actual dielectric profile is used, it predicts the scattered field to an accuracy which is adequate for most practical purposes.

Contents

1 Introduction 1

2 Structure of a Leaf 2

3 Physical Optics Approximations 4

4 Combined Sheets Model 11

5 Scattering by a Stack of N Planar Sheets 12

5.1 E-Polarization 14

5.2 H-Polarization 16

6 Scattering by a Rectangular Stack 18

6.1 E-polarization 20

6.2 H-polarization 21

7 Numerical Results 22

8 Conclusions 25

A APPENDIX A Two Dimensinal Scattering by Cylindrical Structures with High Refractive Index A-1

1 Introduction A-1

2 Formulation A-3

3 Numerical Analysis **A-5**

4 Extension to Three-Dimensional Scattering **A-11**

List of Figures

1 The structure of a typical vegetation leaf. 3

2 The geometry of the scattering of a plane wave from a two-layer dielectric slab. 6

3 N layer of combined-sheets simulating infinite dielectric slab. 12

4 The geometry of scattering of a plane wave from a finite N-layer combined-sheet. 19

5 Amplitude of the ratio of the bistatic far field amplitude of VIPO to SCPO for E polarization of a dielectric plate with $d_2 = \lambda_0/4$ and $\epsilon_1 = \epsilon_2 = 3 + i0.1$ at $\theta_0 = 30$ degrees. 30

6 Phase of the ratio of the bistatic far field amplitude of VIPO to SCPO for E polarization of a dielectric plate with $d_2 = \lambda_0/4$ and $\epsilon_1 = \epsilon_2 = 3 + i0.1$ at $\theta_0 = 30$ degrees. 31

7 The bistatic cross section of a $2\lambda_0 \times 2\lambda_0$ plate for E polarization with $d_2 = \lambda_0/4$ and $\epsilon_1 = \epsilon_2 = 3 + i0.1$ at normal incidence: (——) moment method solution, (- - -) VIPO, (– –) SCPO. 32

8 The bistatic cross section area of a $2\lambda_0 \times 2\lambda_0$ plate for E polarization with $d_2 = \lambda_0/50$ and $\epsilon_{avg} = 13 + i12$ at normal incidence: (——) moment method solution, (- - -) VIPO or SCPO. 33

9 The bistatic cross section of a $2\lambda_0 \times 2\lambda_0$ plate for H polarization with $d_2 = \lambda_0/50$ and $\epsilon_{avg} = 13 + i12$ at normal incidence: (——) moment method solution, (- - -) VIPO or SCPO. 34

10 The bistatic cross section of a $1.4\lambda_0 \times 2\lambda_0$ plate for E polarization with $d_2 = 2d_1 = 0.5mm$ and f =140 GHz at normal incidence: (——) moment method solution with $\epsilon_1 = 5+i4$, $\epsilon_2 = 2+i1$, (- - -) VIPO with $\epsilon_1 = 5 + i4$, $\epsilon_2 = 2 + i1$, (– –) VIPO with $\epsilon_2 = \epsilon_1 = 3.5 + i2.5$. 35

11 The bistatic cross section area of a $1.4\lambda_0 \times 2\lambda_0$ plate for H polarization with $d_2 = 2d_1 = 0.5mm$ and f =140 GHz at normal incidence: (——) moment method solution with $\epsilon_1 = 5 + i4$, $\epsilon_2 = 2 + i1$, (- - -) VIPO with $\epsilon_1 = 5+i4$ $\epsilon_2 = 2+i1$, (– –) VIPO with $\epsilon_2 = \epsilon_1 = 3.5+i2.5$. 36

12 Amplitude of the reflection coefficient at f=35GHz, $\theta_0 = 0$,and $\epsilon = 13 + i12$ as a function of thickness: (——) exact solution, (- - -) N-layered combined-sheet model $\Delta = \lambda/100$, (– –) single-sheet $\Delta = \tau$. 37

13 Phase of the reflection coefficient at f=35GHz, $\theta_0 = 0$,and $\epsilon = 13 + i12$ as a function of thickness: (——) exact solution, (- - -) N-layered combined-sheet model $\Delta = \lambda/100$, (– –) single-sheet $\Delta = \tau$. 38

14 Bistatic scattering cross section of a $2\lambda \times 2\lambda$ dielectric plate with $\tau = \lambda/100$ for E-polarization at f=35GHz, $\theta_0 = 0$, and $\epsilon = 13+i12$ as function of scattering angle: (——) moment method, (- - -) single-layered combined-sheet model. 39

15 Bistatic scattering cross section of a $2\lambda \times 2\lambda$ dielectric plate with $\tau = \lambda/100$ for H-polarization at f=35GHz, $\theta_0 = 0$, and $\epsilon = 13+i12$ as function of scattering angle: (——) moment method, (- - -) single-layered combined-sheet model. 40

16 Bistatic scattering cross section of a $1\lambda \times 2\lambda$ dielectric plate with $\tau = \lambda/10$ for E-polarization at f=35GHz, $\theta_0 = 0$, and $\epsilon = 13+i12$ as function of scattering angle: (——) moment method, (- - -) 5-layered combined-sheet model, (– –) single-sheet. 41

17 Bistatic scattering cross section of a $1\lambda \times 2\lambda$ dielectric plate with $\tau = \lambda/10$ for H-polarization at f=35GHz, $\theta_0 = 0$, and $\epsilon = 13+i12$ as function of scattering angle: (——) moment method, (- - -) 5-layered combined-sheet model, (– –) single-sheet. 42

1 Introduction

Leaves are a key feature of any vegetation canopy , and in order to model the scattering from vegetation-covered land, it is necessary to develop an efficient and effective technique for predicting the scattering from a single leaf. At microwave frequencies where a typical leaf is electrically thin with lateral dimensions at least comparable to the free space wavelength λ_0, several methods have been proposed [e.g. Le Vine et al 1985, Willis et al, 1988] all based on the physical optics approximation applied to a uniform dielectric slab. In particular, if the leaf thickness is no more than about $\lambda_0/50$, physical optics in conjunction with a resistive sheet model predicts the scattering at most angles of incidence [Senior et al, 1987] and can also handle curved leaves [Sarabandi et al, 1988].

On the other hand, at millimeter wavelengths the thickness can be a significant fraction of a wavelength, and it is also necessary to take into account the internal structure of a leaf. At least two different types of cell can be distinguished, and their differing water content affects the dielectric constant, leading to a nonuniform dielectric profile. To compute the scattering at these higher frequencies, two different physical optics approximations are examined. The first of these employs the polarization current which would exist in an infinite slab consisting of one, two or more layers simulating the dielectric profile of the leaf, and this is referred to as the volume integral physical optics (VIPO) approximation. When there are many layers, a convenient method of implementation is described in the Appendix. The second (and simpler) approach postulates a surface current which, for an infinite

slab, produces a plane wave identical to the reflected field, and this is the surface current physical optics (SCPO) approximation.

For an electrically thin leaf or plate, the two approximations are indistinguishable, but as the thickness (or frequency) increases, the predicted scattering differs in most directions, and by comparison with the results of a moment method solution of the volume integral equation, it is shown that VIPO is superior. In addition, for a two layer material, it is no longer adequate to treat the plate as homogeneous one having an average dielectric constant. Provided the actual dielectric profile of a leaf is simulated, it appears that VIPO can predict the scattering behavior of a leaf to an accuracy that is sufficient for most practical purposes at millimeter wavelengths.

2 Structure of a Leaf

The structure of a typical vegetation leaf is shown in Fig.1. The type and number density of cells may vary as a function of depth into the leaf which, in turn, results in a nonuniform dielectric profile. The effect of this nonuniformity becomes observable at higher frequencies where the thickness of the leaf is comparable to the wavelength.

Leaves contain two types of photosynthetic cells: *palisade parenchyma*, consisting of column-shaped cells in which most photosynthesis takes place, and *spongy parenchyma*, which consist of irregularly shaped cells with large spaces between them. Because a large part of the vegetation material is water, its dielectric con-

stant is strongly influenced by the dielectric constant of water and the water content. For most leaves, the water content is higher in its upper layer (palisade region) than in the under surface (spongy region).

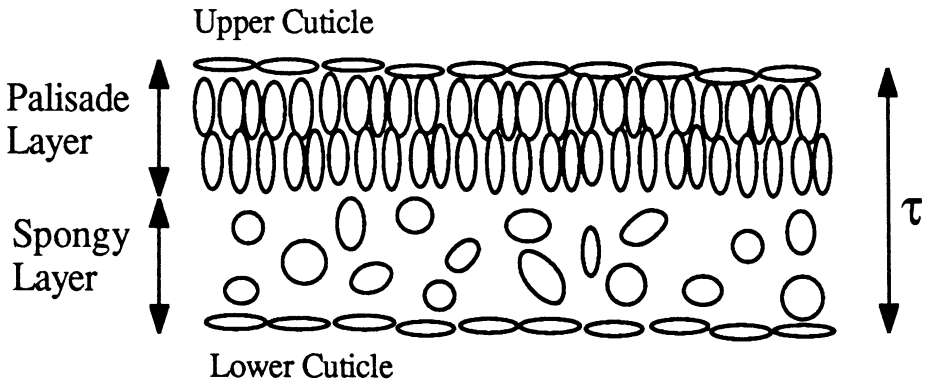

Figure 1: The structure of a typical vegetation leaf.

The sensitivity of the dielectric constant to water content is much greater in the lower part of the millimeter wave spectrum than in the upper, but this is more than counterbalanced by the thickness to wavelength ratio. The net result is that the sensitivity to dielectric variations is greater at the higher frequencies.

To examine the effect of the nonuniform dielectric profile on the scattering properties of the leaf at millimeter wavelengths, we computed the normal incidence reflection coefficient Γ_0 of a two-layer dielectric slab and compared it with the reflection coefficient of a uniform dielectric slab whose dielectric constant is the

average. The computation was performed for a leaf thickness of $0.5mm$, and the water content ratio of the two layer was chosen to be 4 to 1, representing a marked variation between the upper and lower surfaces of the leaf. From the data in Table 1, it is seen that when the two-layer slab is approximated by a uniform slab the

f (GHz)	ϵ_1	ϵ_2	$\epsilon_{(avg)} = \frac{\epsilon_1+\epsilon_2}{2}$	Γ_0	$\Gamma_{0(avg)}$
35	20+i21	6+i3	13+i12	$0.74\angle 6$	$0.78\angle -0.16$
94	6+i5	2+i1	4+i3	$0.59\angle 12$	$0.48\angle 27$
140	5+i4	2+i1	3.5+i2.5	$0.50\angle 20$	$0.34\angle 26.1$

Table 1: Voltage reflection coefficient for a two-layer and average dielectric slab

error in the reflection coefficient increases with increasing frequency, and is as large as 4 dB at 140 GHz.

3 Physical Optics Approximations

At microwave frequencies where a typical leaf is no more than about $\lambda_0/50$ in thickness with lateral dimensions comparable to or larger than the wavelength, the scattering properties can be accurately predicted using the physical optics approximation applied to a resistive sheet model of a leaf [Sarabandi et al, 1988]. In effect, the leaf is modeled as an infinitesimally thin layer, but as the frequency increases, it is necessary to take the leaf thickness in to account. There are now two types of physical optics approximation that can be employed. The standard one is the surface current (SCPO) approach in which an infinite dielectric slab is replaced

by an equivalent sheet current that produces a plane wave identical to the reflected wave of the slab. This current is then used as an approximation to the equivalent surface current over the upper surface of a finite dielectric plate. Alternatively, the induced (volume) polarization current in the plate can be approximated by the current in the infinite dielectric slab, and we shall refer to this as the volume integral physical optics (VIPO) method. It is more accurate than the SCPO method, although the latter is more convenient to use for evaluating the scattered field.

To illustrate the two procedures, consider a dielectric plate consisting of a homogeneous dielectric of thickness d_1 and relative permittivity ϵ_1 atop a second material of thickness $d_2 - d_1$ and relative permittivity ϵ_2. The plate occupies the region $-\frac{a}{2} \leq y \leq \frac{a}{2}$, $-\frac{b}{2} \leq y \leq \frac{b}{2}$, and $-d_2 \leq z \leq 0$ as shown in Fig. 2, and is illuminated by an E-polarized plane wave whose electric vector is

$$\mathbf{E}^i = \hat{\mathbf{y}} e^{ik_0(x\sin\theta_0 - z\cos\theta_0)} \tag{1}$$

where k_0 is the propagation constant in the free space medium above and below the plate. When the plate is treated as an infinitely extended slab, the electric field can be written as

$$\begin{aligned}
E_y = &\ (e^{-ik_{0z}z} + \Gamma e^{ik_{0z}z})e^{ik_0\sin\theta_0 x} && (0 \leq z) \\
E_y = &\ (B_1 e^{-ik_{1z}z} + A_1 e^{ik_{1z}z})e^{ik_0\sin\theta_0 x} && (-d_1 \leq z \leq 0) \\
E_y = &\ (B_2 e^{-ik_{2z}z} + A_2 e^{ik_{2z}z})e^{ik_0\sin\theta_0 x} && (-d_2 \leq z \leq -d_1) \\
E_y = &\ B_3 e^{-ik_{0z}z} e^{ik_0\sin\theta_0 x} && (z \leq -d_2)
\end{aligned} \tag{2}$$

where

$$k_{0z} = k_0\cos\theta_0, \qquad k_{jz} = k_0\sqrt{\epsilon_j - \sin^2\theta_0}$$

for $j = 1, 2$.

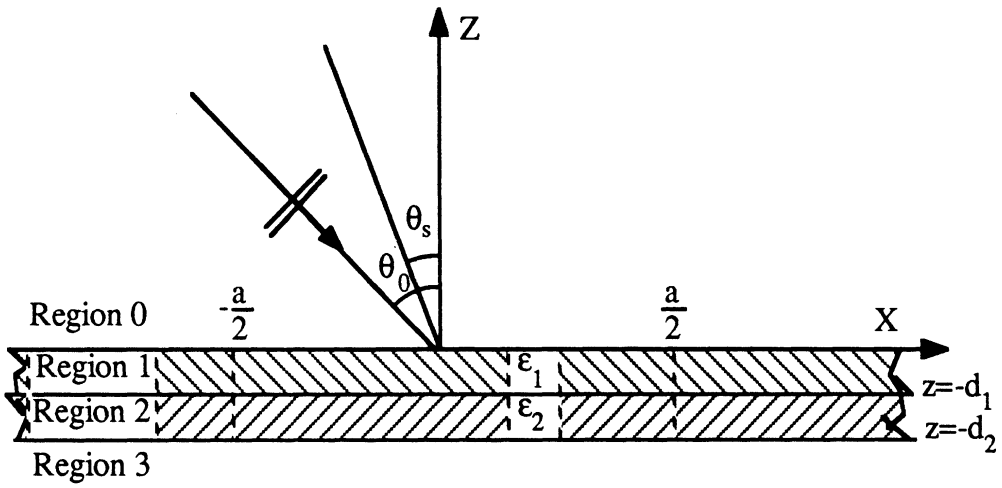

Figure 2: The geometry of the scattering of a plane wave from a two-layer dielectric slab.

If R_1 and R_2 are the reflection coefficients at the upper and lower surfaces where

$$R_1 = \frac{k_{0z} - k_{1z}}{k_{0z} + k_{1z}}, \qquad R_2 = \frac{k_{0z} - k_{2z}}{k_{0z} + k_{2z}}$$

and

$$C_\pm = 1 \pm \frac{k_{2z}}{k_{1z}} \left\{1 + R_2 e^{2ik_{2z}(d_2 - d_1)}\right\} \left\{1 - R_2 e^{2ik_{2z}(d_2 - d_1)}\right\}^{-1},$$

application of the boundary condition at the three interfaces gives

$$B_1 = \frac{C_+(1+R_1)}{C_+ + C_- R_1 e^{2ik_{1z}d_1}}, \qquad A_1 = \frac{C_-}{C_+} e^{2ik_{1z}d_1} B_1 \tag{3}$$

$$B_2 = \frac{e^{i(k_{1z}-k_{2z})d_1}}{1 - R_2 e^{2ik_{2z}(d_2-d_1)}} \cdot \frac{2}{C_+} B_1, \quad A_2 = -R_2 e^{2ik_{2z}d_2} B_2 \tag{4}$$

$$B_3 = e^{i(k_{2z}-k_{0z})d_2}(1 - R_2) B_2$$

and

$$\Gamma = \frac{C_+ R_1 + C_- e^{2ik_{1z}d_1}}{C_+ + C_- R_1 e^{2ik_{1z}d_1}}. \tag{5}$$

The corresponding results for a single layer of thickness d_1 and relative dielectric constant ϵ_1 can be obtained by putting $d_2 = d_1$ and $k_{2z} = k_{1z}$, implying $B_2 = B_1$ and $A_2 = A_1$.

Given a volume distribution of electric ($\mathbf{J}$) and magnetic ($\mathbf{J}^*$) current in free space, the corresponding Hertz vector are

$$\begin{aligned} \mathbf{\Pi}(\bar{r}) = &\ \tfrac{iZ_0}{4\pi k_0} \textstyle\int_V \mathbf{J}(\bar{r}') \tfrac{e^{ik_0|\bar{r}-\bar{r}'|}}{|\bar{r}-\bar{r}'|} \mathrm{d}v, \\ \mathbf{\Pi}^*(\bar{r}) = &\ \tfrac{iY_0}{4\pi k_0} \textstyle\int_V \mathbf{J}^*(\bar{r}') \tfrac{e^{ik_0|\bar{r}-\bar{r}'|}}{|\bar{r}-\bar{r}'|} \mathrm{d}v, \end{aligned} \tag{6}$$

where $Z_0 (= 1/Y_0)$ is the free space impedance, and the resulting fields are

$$\begin{aligned} \mathbf{E}(\bar{r}) = &\ \nabla \times \nabla \times \mathbf{\Pi}(\bar{r}) + ik_0 Z_0 \nabla \times \mathbf{\Pi}^*, \\ \mathbf{H}(\bar{r}) = &\ -ik_0 Y_0 \nabla \times \mathbf{\Pi}(\bar{r}) + \nabla \times \nabla \times \mathbf{\Pi}^*. \end{aligned}$$

In the far zone of the current distribution

$$\begin{aligned} \mathbf{\Pi}(\bar{r}) \approx &\ \tfrac{e^{ik_0 r}}{k_0 r} \tfrac{iZ_0}{4\pi} \textstyle\int_V \mathbf{J}(\bar{r}') e^{-ik_0 \hat{r}\cdot\bar{r}'} \mathrm{d}v, \\ \mathbf{\Pi}^*(\bar{r}) \approx &\ \tfrac{e^{ik_0 r}}{k_0 r} \tfrac{iY_0}{4\pi} \textstyle\int_V \mathbf{J}^*(\bar{r}') e^{-ik_0 \hat{r}\cdot\bar{r}'} \mathrm{d}v, \end{aligned} \tag{7}$$

and

$$\begin{aligned} \mathbf{E}(\bar{r}) \approx &\ -k_0^2 [\hat{\mathbf{r}} \times \hat{\mathbf{r}} \times \mathbf{\Pi}(\bar{r}) + Z_0 \hat{\mathbf{r}} \times \mathbf{\Pi}^*(\bar{r})], \\ \mathbf{H}(\bar{r}) \approx &\ -k_0^2 [\hat{\mathbf{r}} \times \hat{\mathbf{r}} \times \mathbf{\Pi}^*(\bar{r}) + Y_0 \hat{\mathbf{r}} \times \mathbf{\Pi}(\bar{r})]. \end{aligned} \tag{8}$$

In the dielectric slab the volume current $\mathbf{J}$ is the polarization current

$$\mathbf{J} = -ik_0 Y_0 (\epsilon_j - 1) E_y \hat{\mathbf{y}}. \tag{9}$$

where E_y has the value appropriate to each layer ($j = 1, 2$), and when this is inserted into (6) and the integration carried out over the volume occupied by the plate, we obtain the VIPO approximation. For scattering in the direction θ_s indicated in Fig. 2 the expression for the Hertz vector is

$$\mathbf{\Pi}^{VIPO} = \hat{\mathbf{y}} \frac{e^{ik_0 r}}{k_0 r} \frac{k_0 ab}{4\pi} \frac{\sin X}{X} F \tag{10}$$

where

$$\begin{aligned} F = \; & (\epsilon_1 - 1) \left\{ \frac{1 - e^{-i(k_{1z} - k_0 \cos\theta_s) d_1}}{i(k_{1z} - k_0 \cos\theta_s)} A_1 - \frac{1 - e^{-i(k_{1z} + k_0 \cos\theta_s) d_1}}{i(k_{1z} + k_0 \cos\theta_s)} B_1 \right\} \\ & + (\epsilon_2 - 1) \{ \frac{e^{-i(k_{2z} - k_0 \cos\theta_s) d_1} - e^{-i(k_{1z} - k_0 \cos\theta_s) d_2}}{i(k_{2z} - k_0 \cos\theta_s)} A_2 \\ & - \frac{e^{i(k_{2z} + k_0 \cos\theta_s) d_1} - e^{-i(k_{2z} + k_0 \cos\theta_s) d_2}}{i(k_{2z} + k_0 \cos\theta_s)} B_2 \} \end{aligned} \tag{11}$$

and

$$X = \frac{k_0 a}{2} (\sin\theta_s + \sin\theta_0). \tag{12}$$

The far zone scattered field can then be obtained from (7) and written as

$$\mathbf{E}^s = \frac{e^{ik_0 r}}{k_0 r} \mathbf{S}_E(\theta_s, \theta_0) \tag{13}$$

where $\mathbf{S}_E(\theta_s, \theta_0)$ is the far field amplitude, and for the VIPO approximation the result is

$$\mathbf{S}_E^{VIPO}(\theta_s, \theta_0) = \hat{\mathbf{y}} \frac{k_0^3 ab}{4\pi} \frac{\sin X}{X} F. \tag{14}$$

In terms of the far field amplitude, the bistatic scattering cross section is

$$\sigma(\theta_S, \theta_0) = \frac{\lambda_0^2}{\pi} \mid \mathbf{S}(\theta_s, \theta_0) \mid^2 . \tag{15}$$

The more conventional SCPO approximation can be obtained by noting that the electric current sheet

$$\mathbf{J} = -2Y_0 \cos\theta_0 \Gamma e^{ik_0 \sin\theta_0 x}\delta(z)\hat{\mathbf{y}} \tag{16}$$

produces a plane wave identical to the field reflected from the dielectric slab. As evident from the impulse function $\delta(z)$ in (16), the current is located at the upper surface of the slab, and when (16) is inserted into (6) we find

$$\mathbf{\Pi}^{SCPO} \approx \hat{\mathbf{y}}\frac{e^{ik_0 r}}{k_0 r}\cdot\frac{-i}{2\pi}\cos\theta_0\Gamma ab\frac{\sin X}{X}, \tag{17}$$

and the far field amplitude is then

$$\mathbf{S}_E^{SCPO}(\theta_s,\theta_0) = \hat{\mathbf{y}}\frac{-ik_0^2}{2\pi}\cos\theta_0\Gamma ab\frac{\sin X}{X}. \tag{18}$$

In the specular ($\theta_s = -\theta_0$) and backscattering ($\theta_s = \theta_0$) directions it can be verified that (14) and (18) are identical, but in the other directions the two approximations differ.

In the case of H polarization for which

$$\begin{aligned}\mathbf{E}^i &= -Z_0(\cos\theta_0\hat{\mathbf{x}} + \sin\theta_0\hat{\mathbf{z}})e^{ik_0(x\sin\theta_0 - z\cos\theta_0)},\\ \mathbf{H}^i &= \hat{\mathbf{y}}e^{ik_0(x\sin\theta_0 - z\cos\theta_0)}.\end{aligned} \tag{19}$$

the analysis is similar. With H_y represented as shown in (2), the various coefficients (now indicated by primes) differ from those for E polarization in having k_{1z} replaced by k_{1z}/ϵ_1 and k_{2z} replaced by k_{2z}/ϵ_2 everywhere except in the exponents. The induced polarization current then has two components and is given by

$$\mathbf{J} = -ik_0 Z_0(\epsilon_j - 1)(E_x\hat{\mathbf{x}} + E_z\hat{\mathbf{z}}). \tag{20}$$

where $E_x = (ik_0\epsilon_j)^{-1}Z_0\partial H_y/\partial x$ and $E_z = -(ik_0\epsilon_j)^{-1}Z_0\partial H_y/\partial x$ have the values appropriate to each layer ($j = 1, 2$). The Hertz vector can be computed using (6), and for the scattered field $\mathbf{H}^s$, the far field amplitude is found to be

$$\mathbf{S}_H^{VIPO}(\theta_s, \theta_0) = \hat{\mathbf{y}}\frac{k_0^3 ab}{4\pi}\frac{\sin X}{X}(\cos\theta_s F_1' - \sin\theta_s F_2'). \tag{21}$$

where

$$\begin{aligned} F_1' = \; & \{\tfrac{k_{1z}(\epsilon_1-1)}{k_0\epsilon_1}\left[\tfrac{1-e^{-i(k_{1z}-k_0\cos\theta_s)d_1}}{i(k_{1z}-k_0\cos\theta_s)}A_1' + \tfrac{1-e^{i(k_{1z}+k_0\cos\theta_s)d_1}}{i(k_{1z}+k_0\cos\theta_s)}B_1'\right] \\ & + \tfrac{k_{2z}(\epsilon_2-1)}{k_0\epsilon_2}\left[\tfrac{e^{-i(k_{2z}-k_0\cos\theta_s)d_1} - e^{-i(k_{1z}-k_0\cos\theta_s)d_2}}{i(k_{2z}-k_0\cos\theta_s)}A_2'\right. \\ & \left. + \tfrac{e^{i(k_{2z}+k_0\cos\theta_s)d_1} - e^{-i(k_{2z}+k_0\cos\theta_s)d_2}}{i(k_{2z}+k_0\cos\theta_s)}B_2'\right]\}, \end{aligned} \tag{22}$$

and

$$\begin{aligned} F_2' = \; & \sin\theta_0\{\tfrac{(\epsilon_1-1)}{\epsilon_1}\left[\tfrac{1-e^{-i(k_{1z}-k_0\cos\theta_s)d_1}}{i(k_{1z}-k_0\cos\theta_s)}A_1' - \tfrac{1-e^{i(k_{1z}+k_0\cos\theta_s)d_1}}{i(k_{1z}+k_0\cos\theta_s)}B_1'\right] \\ & + \tfrac{(\epsilon_2-1)}{\epsilon_2}\left[\tfrac{e^{-i(k_{2z}-k_0\cos\theta_s)d_1} - e^{-i(k_{1z}-k_0\cos\theta_s)d_2}}{i(k_{2z}-k_0\cos\theta_s)}A_2'\right. \\ & \left. - \tfrac{e^{i(k_{2z}+k_0\cos\theta_s)d_1} - e^{-i(k_{2z}+k_0\cos\theta_s)d_2}}{i(k_{2z}+k_0\cos\theta_s)}B_2'\right]\}. \end{aligned} \tag{23}$$

The SCPO approximation can also be obtained by noting that a magnetic current sheet of the form

$$\mathbf{J}^* = -2Z_0\cos\theta_0\Gamma' e^{ik_0\sin\theta_0 x}\delta(z)\hat{\mathbf{y}} \tag{24}$$

generates a plane wave identical to the reflected wave. Using this as the equivalent surface current on the dielectric plate, the magnetic far field amplitude becomes

$$\mathbf{S}_H^{SCPO}(\theta_s, \theta_0) = \hat{\mathbf{y}}\frac{-ik_0^2}{2\pi}\cos\theta_0\Gamma' ab\frac{\sin X}{X}. \tag{25}$$

As in the case of E polarization, the two approximations are identical in the specular direction, but (21) and (25) differ in all other directions, including backscattering ($\theta_s = \theta_0$) unless $\theta_0 = 0$.

4 Combined Sheets Model

When using the VIPO approximation, an efficient way to take into account the effect of any non-uniformity in the dielectric profile is to model the leaf as a stack of N combined current sheets. Each sheet simulates a very thin dielectric layer whose thickness is less than $\lambda/15$ where λ is the wavelength in the material. A combined sheet consists of coincident resistive and modified conductive sheets that support electric and magnetic currents respectively, with the conductive sheet accounting for the electric currents flowing perpendicular to the dielectric layer. The m^{th} layer sheets are characterized by a complex resistivity and conductivity R_m and R_m^*, respectively, where

$$\begin{aligned} R_m &= \frac{iZ_0}{k_0 \Delta_m (\epsilon_m - 1)} \\ R_m^* &= \frac{iY_0 \epsilon_m}{k_0 \Delta_m (\epsilon_m - 1)}. \end{aligned} \tag{26}$$

Here ϵ_m and Δ_m are the relative dielectric constant and thickness of the m^{th} layer, and $\tau = \sum_{m=1}^{N} \Delta_m$ is the total thickness of the dielectric slab.

The boundary conditions at the m^{th} combined sheet are as follows [Senior and Volakis; 1987]:

$$\hat{\mathbf{n}} \times \{\hat{\mathbf{n}} \times [\mathbf{E}^+ + \mathbf{E}^-]\} = -2R_m \mathbf{J}_m \tag{27}$$

$$\mathbf{J}_m = \hat{\mathbf{n}} \times [\mathbf{H}^+ - \mathbf{H}^-] \tag{28}$$

where $\mathbf{J}_m$ is the total electric current supported by the resistive sheet, and

$$\hat{\mathbf{n}} \times \{\hat{\mathbf{n}} \times [\mathbf{H}^+ + \mathbf{H}^-]\} - \frac{iY_0}{k_0}\hat{\mathbf{n}} \times \frac{\partial}{\partial n}[\mathbf{E}^+ + \mathbf{E}^-] = -2R_m^* \mathbf{J}_m^* \tag{29}$$

$$\mathbf{J}_m^* = -\hat{\mathbf{n}} \times [\mathbf{E}^+ - \mathbf{E}^-] \tag{30}$$

where $\mathbf{J}_m^*$ is the total magnetic current supported by the conductive sheet. The superscripts $^{+,-}$ refer to the upper $(+)$ and lower $(-)$ sides of the sheet, and $\hat{\mathbf{n}}$ is the unit vector outward normal to the upper side.

5 Scattering by a Stack of N Planar Sheets

Consider a stack of N infinite planar combined sheets that are all parallel to the $x-y$ plane of a Cartesian coordinate system (x, y, z) as depicted in Fig. 3.

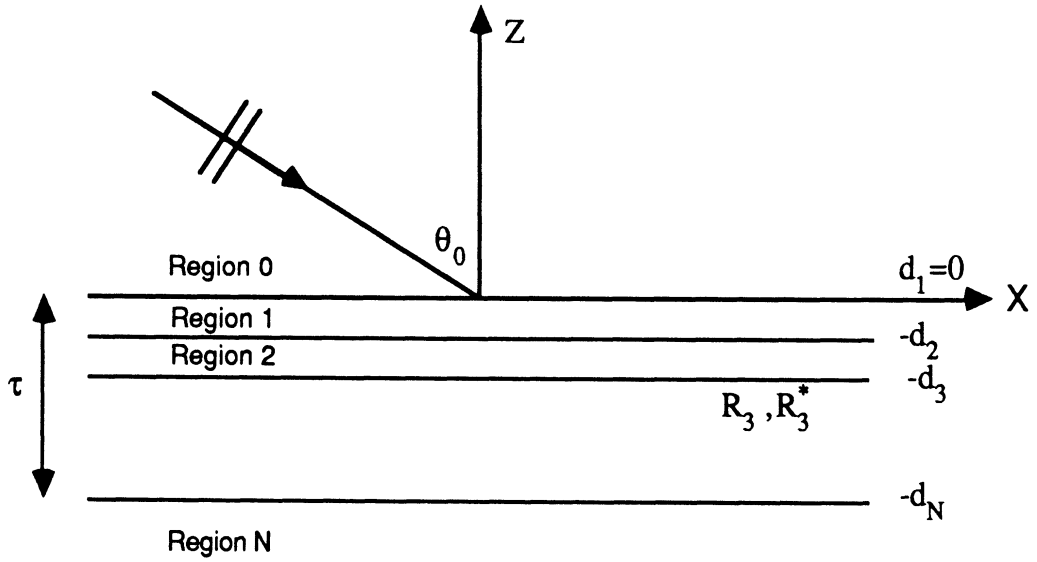

Figure 3: N layer of combined-sheets simulating infinite dielectric slab.

The top sheet is in the $z = 0$ plane and the m^{th} sheet is located at $z = -d_m$, where

$d_1 = 0$. The space between the m^{th} and $(m+1)^{th}$ sheets is denoted by region m, and we note that region 0 ($z > 0$) and region N ($z < -d_n$) are semi-infinite free space. A plane wave whose plane of incidence is parallel to the $x - z$ plane impinges on the stack of sheets from above. From the symmetry of the problem, all the field vectors are independent of $y(i.e., \frac{\partial}{\partial y} = 0)$, as a result of which the field components in each region can be separated into $E-$ and $H-$polarized waves which are the dual of each other. From Maxwell's equation the field components in region m for an E-polarized wave must satisfy

$$H_{mx} = -\frac{1}{i\omega\mu_0}\frac{\partial}{\partial z}E_{my}, \tag{31}$$

$$H_{mz} = \frac{1}{i\omega\mu_0}\frac{\partial}{\partial x}E_{my}, \tag{32}$$

$$(\frac{\partial^2}{\partial x^2} + \frac{\partial^2}{\partial z^2} + k^2)E_{my} = 0, \tag{33}$$

and for a H-polarized wave

$$E_{mx} = \frac{1}{i\omega\epsilon_0}\frac{\partial}{\partial z}H_{my}, \tag{34}$$

$$E_{mz} = -\frac{1}{i\omega\epsilon_0}\frac{\partial}{\partial x}H_{my}, \tag{35}$$

$$(\frac{\partial^2}{\partial x^2} + \frac{\partial^2}{\partial z^2} + k^2)H_{my} = 0. \tag{36}$$

Equations (34)-(39) are the dual of (31)-(33) and each can be obtained from the other on replacing E_m by H_m, H_m by $-E_m$, and $\epsilon_0(\mu_0)$ by $\mu_0(\epsilon_0)$.

5.1 E-Polarization

For the case of E polarization in which the electric field vector of the incident wave is perpendicular to the plane of incidence, the incident field is given by (1). From (33), (31) and (32) the field vector in region m can be expressed as

$$E_{my} = [C_m^i e^{-ik_0 \cos\theta_0 z} + C_m^r e^{ik_0 \cos\theta_0 z}] e^{ik \sin\theta_0 x} \tag{37}$$

$$H_{mx} = Y_0 \cos\theta_0 [C_m^i e^{-ik_0 \cos\theta_0 Z} - C_m^r e^{ik_0 \cos\theta_0 z}] e^{ik_0 \sin\theta_0 x} \tag{38}$$

$$H_{mz} = Y_0 \sin\theta_0 [C_m^i e^{-ik_0 \cos\theta_0 z} + C_m^r e^{ik_0 \cos\theta_0 z}] e^{ik_0 \sin\theta_0 x} \tag{39}$$

The coefficients C_m^i and C_m^r are the amplitudes of the waves travelling in the $-z$ and $+z$ directions, respectively, in region m. In region 0, $C_0^i = 1$ and $C_0^r = \Gamma_E$ (the total reflection coefficient) and in region N, $C_N^r = 0$, $C_N^i = T_E$ (the total transmission coefficient). Hence, using the boundary conditions (27)-(30), there are $2N$ unknowns and $2N$ equations that can be solved simultaneously. The quantities of primary interest are the total reflection and transmission coefficients which can be obtained directly as follows. From boundary condition (29) we have

$$\hat{\mathbf{z}} \times \left\{ \hat{\mathbf{z}} \times \hat{\mathbf{x}} [H_{(m-1)x} + H_{mx}] \right\} - \frac{iY_0}{k_0} \hat{\mathbf{z}} \times \frac{\partial}{\partial z} [E_{(m-1)y} + E_{my}] = -2R_m^* \mathbf{J}_m^* \tag{40}$$

Upon substitution of (37) and (38) into (40) the left hand side of (40) vanishes resulting in $\mathbf{J}_m^* = 0$. Thus, the conductive sheet is not excited in this polarization, as expected since there is no current in the z direction in the dielectric slab. In the absence of a magnetic source the tangential component of the electric field must

be continuous as given by (30)

$$\left(E_{(m-1)y} - E_{my}\right) |_{z=-d_m} = 0 \tag{41}$$

Upon inserting the expressions (37) and (38) into (41), (27), and (28) the following set of equations is obtained

$$C^i_{(m-1)} e^{ik_0 \cos\theta_0 d_m} + C^r_{(m-1)} e^{-ik_0 \cos\theta_0 d_m} = C^i_m e^{ik_0 \cos\theta_0 d_m} + C^r_m e^{-ik_0 \cos\theta_0 d_m} \tag{42}$$

$$C^i_m e^{ik_0 \cos\theta_0 d_m} + C^r_m e^{-ik_0 \cos\theta_0 d_m} =$$

$$Y_0 \cos\theta_0 R_m [C^i_{(m-1)} e^{ik_0 \cos\theta_0 d} - C^r_{(m-1)} e^{-ik_0 \cos\theta_0 d_m} - C^i_m e^{ik_0 \cos\theta_0 d_m} + C^r_m e^{-ik \cos\theta_0 d_m}] \tag{43}$$

By defining the reflection coefficient in region m as

$$\Gamma^E_m \triangleq \frac{C^r_m}{C^i_m} e^{-2ik_0 \cos\theta_0 d_{m+1}},$$

the following relations can be obtained:

$$\Gamma^E_{m-1} = \frac{-1 + (2Y_0 \cos\theta_0 R_{m-1})\, e^{2ik_0 \cos\theta_0 (d_{m+1} - d_m)} \Gamma^E_m}{(1 + 2Y_0 \cos\theta_0 R_m) + e^{2ik_0 \cos\theta_0 (d_{m+1} - d_m)} \Gamma^E_m} \tag{44}$$

$$C^i_m = \frac{1 + \Gamma^E_{m-1}}{1 + e^{2ik_0 \cos\theta_0 (d_{m+1} - d_m)} \Gamma^E_m} C^i_{m-1} \tag{45}$$

The induced electric current in the m^{th} sheet can also be obtained from (28) and by application of (42) it can be expressed as (excluding the phase factor $e^{ik_0 \sin\theta_0 x}$)

$$\mathbf{J}^E_m = \hat{\mathbf{y}} 2Y_0 \cos\theta_0 \left[C^r_m - C^r_{m-1}\right] e^{-ik_0 \cos\theta_0 d_m} \tag{46a}$$

This induced current may be expressed in terms of the reflection coefficients of

different layers:

$$\begin{aligned}\mathbf{J}_m^E = & \ \hat{\mathbf{y}} 2Y_0 \cos\theta_0 [C_{m-1}^i - C_m^i] e^{ik_0 \cos\theta_0 d_m} \\ & = \hat{\mathbf{y}} 2Y_0 \cos\theta_0 e^{ik_0 \cos\theta_0 d_m} [1 - \tfrac{1+\Gamma_m^E}{1+e^{2ik_0\cos\theta_0(d_{m+1}-d_m)}\Gamma_m^E}] \\ & \cdot \textstyle\prod_{\ell=1}^{m-1} (\tfrac{1+\Gamma_{\ell-1}^E}{1+e^{2ik_0\cos\theta_0(d_{\ell+1}-d_\ell)}\Gamma_\ell^E})\end{aligned} \tag{46b}$$

Now, the total reflection coefficient in region 0 ($\Gamma_E(\theta) = \Gamma_0^E$) can be evaluated from the recursive relation (44) by noting that $\Gamma_N^E = 0$ (the region N is semi-infinite). The total transmission coefficient can also be obtained from (45) and (44) as follows:

$$T_E(\theta) \triangleq \frac{C_N^i}{C_0^i} = \prod_{m=1}^{N} \left[\frac{1+\Gamma_{m-1}^E}{1+e^{2ik_0\cos\theta_0(d_{m+1}-d_m)}\Gamma_m^E} \right] \tag{47}$$

5.2 H-Polarization

Unlike the E-polarized case where the magnetic current is zero, an H-polarized incident wave excites a magnetic current in the y direction and neither of the tangential electric or magnetic field is continuous across the combined sheets. The tangential field vectors in region m can be obtained by applying the duality relationships to equation (37) and (38). Therefore,

$$H_{my} = \left[B_m^i e^{-ik_0\cos\theta_0 z} + B_m^r e^{ik_0\cos\theta_0 z} \right] e^{ik_0 \sin\theta_0 x} \tag{48}$$

and

$$E_{mx} = -Z_0 \cos\theta_0 \left[B_m^i e^{-ik_0\cos\theta_0 z} - B_m^r e^{ik_0\cos\theta_0 z} \right] e^{ik_0 \sin\theta_0 x} \tag{49}$$

where as before B_m^i and B_m^r are the amplitudes of the waves travelling in $-z$ and $+z$ directions respectively. By applying the boundary conditions (27)-(30) at the

m^{th} sheet and resorting to equations (48) and (49) the following relations between the field amplitudes in region $(m-1)$ and region m are obtained:

$$B^i_{m-1}e^{ik_0\cos\theta_0 d_m} + B^r_{m-1}e^{-ik_0\cos\theta_0 d_m} + B^i_m e^{ik_0\cos\theta_0 d_m} + B^r_m e^{-ik_0\cos\theta_0 d_m} =$$
$$\frac{2R^*_m Z_0\cos\theta_0}{\sin^2\theta_0}\cdot[B^i_{m-1}e^{ik_0 cos\theta_0 d_m} - B^r_{m-1}e^{-ik_0\cos\theta_0 d_m} - B^i_m e^{ik_0\cos\theta_0 d_m} + B^r_m e^{-ik_0\cos\theta 0 d_m}] \tag{50}$$

$$B^i_{m-1}e^{ik_0\cos\theta_0 d_m} - B^r_{m-1}e^{-ik_0\cos\theta_0 d_m} + B^i_m e^{ik_0\cos\theta_0 d_m} - B^r_m e^{-ik_0\cos\theta_0 d_m} =$$
$$\frac{2Rm\sec\theta_0}{z_0}[B^i_{m-1}e^{ik_0\cos\theta_0 d_m} + B^r_{m-1}e^{-ik_0\cos\theta_0 d_m} - B^i_m e^{ik_0\cos\theta_0 d_m} - B^r_m e^{-ik_0\cos\theta 0 d_m}] \tag{51}$$

By denoting the reflection coefficient in region m by

$$\Gamma^H_m \triangleq \frac{B^r_m}{B^i_m}e^{-2ik_0\cos\theta_0 d_{m+1}} \tag{52}$$

after some algebraic manipulation of (50) and (51) we obtain

$$\Gamma^H_{m-1} = \frac{(Q_m P_m - 1) - (1-P_m)(Q_m - 1)\Gamma^H_m e^{2ik_0\cos\theta_0(d_{m+1}-d_m)}}{-(1+P_m)(1+Q_m) + (1-Q_m P_m)\Gamma^H_m e^{2ik_0\cos\theta_0(d_{m+1}-d_m)}} \tag{53}$$

$$B^i_m = \frac{(Q_m - 1) + (1+Q_m)\Gamma^H_{m-1}}{-(1+Q_m) + (1-Q_m)\Gamma^H_m e^{2ik_0\cos\theta_0(d_{m+1}-d_m)}}B^i_{m-1} \tag{54}$$

where the parameters Q_m and P_m are

$$Q_m = \frac{sin^2\theta_0}{2R^*_m Z_0\cos\theta_0}$$
$$P_m = \frac{2R_m\sec\theta_0}{Z_0}.$$

Recursive relation (53) gives the total reflection coefficient in region 0 ($\Gamma_H(\theta) = \Gamma^H_0$) noting that $\Gamma^H_N = 0$ and the total transmission coefficient using (54) is given by

$$T_H(\theta) = \prod_{m=1}^{N}\left[\frac{(Q_m - 1) + (1+Q_m)\Gamma^H_{m-1}}{-(1+Q_m) + (1-Q_m)\Gamma^H_m e^{2ik_0\cos\theta_0(d_{m+1}-d_m)}}\right] \tag{55}$$

The induced electric and magnetic currents in the m^{th} sheet can be obtained by inserting equations (48) and (49) into equations (28) and (30). Excluding the phase factor $e^{ik_0 \sin\theta_0 x}$, they are given by

$$\mathbf{J}_m^H = -(B_{m-1}^i e^{ik_0 \cos\theta_0 d_m} + B_{m-1}^r e^{-ik_0 \cos_0 \theta_0 d_m} - B_m^i e^{ik_0 \cos\theta_0 d_m} - B_m^r e^{-ik_0 \cos\theta_0 d_m})\hat{\mathbf{x}} \tag{56}$$

$$\mathbf{J}_m^{H*} = Z_0 \cos\theta_0 (B_{m-1}^i e^{ik_0 \cos\theta_0 d_m} - B_{m-1}^r e^{-ik_0 \cos_0 \theta_0 d_m} - B_m^i e^{ik_0 \cos\theta_0 d_m} + B_m^r e^{-ik_0 \cos\theta_0 d_m})\hat{\mathbf{y}} \tag{57}$$

after using (52) and (54) the induced currents may be expressed in terms of the reflection coefficients as follows

$$\begin{aligned}\mathbf{J}_m^H = \; & -\hat{\mathbf{x}} e^{ik_0 \cos\theta_0 d_{m-1}}[(1+\Gamma_{m-1}^H) + (1+\Gamma_m^H e^{2ik_0 \cos\theta_0 (d_{m+1}-d_m)}) \\ & \cdot \frac{(Q_m-1)+(1+Q_m)\Gamma_{m-1}^H}{(1+Q_m)+(1-Q_m)\Gamma_m^H e^{ik\cos\theta_0 (d_{m+1}-d_m)}}] \cdot \prod_{\ell=1}^{m-1} [\frac{(Q_\ell-1)+(1+Q_\ell)\Gamma_{\ell-1}^H}{(1+Q_\ell)+(1-Q_\ell)\Gamma_\ell^H e^{ik_0\cos\theta_0 (d_{\ell+1}-d_\ell)}}]\end{aligned} \tag{58}$$

and

$$\begin{aligned}\mathbf{J}_m^{H*} = \; & \hat{\mathbf{y}} Z_0 cos\theta_0 \cdot e^{ik_0 \cos\theta_0 d_{m-1}}[(1-\Gamma_{m-1}^H) + (1-\Gamma_m^H e^{2ik_0 \cos\theta_0 (d_{m+1}-d_m)}) \\ & \cdot \frac{(Q_m-1)+(1+Q_m)\Gamma_{m-1}^H}{(1+Q_m)+(1-Q_m)\Gamma_m^H e^{ik\cos\theta_0 (d_{m+1}-d_m)}}] \cdot \prod_{\ell=1}^{m-1} [\frac{(Q_\ell-1)+(1+Q_\ell)\Gamma_{\ell-1}^H}{(1+Q_\ell)+(1-Q_\ell)\Gamma_\ell^H e^{ik_0\cos\theta_0 (d_{\ell+1}-d_\ell)}}]\end{aligned} \tag{59}$$

Note that here $\mathbf{J}_m^H(x) = \mathbf{J}_m^H e^{ik_0 \sin\theta_0 x}$ and $\mathbf{J}_m^{H*}(x) = \mathbf{J}_m^{H*} e^{ik_0 \sin\theta_0 x}$.

6 Scattering by a Rectangular Stack

Consider a portion of an N-layered stack of combined sheets in the form of a rectangle occupying the region $-\frac{a}{2} \leq x \leq \frac{a}{2}$, $-\frac{b}{2} \leq y \leq \frac{b}{2}$ as depicted in Fig. 4. The illumination and observation directions are such that the planes of incidence and observation are parallel to the x axis.

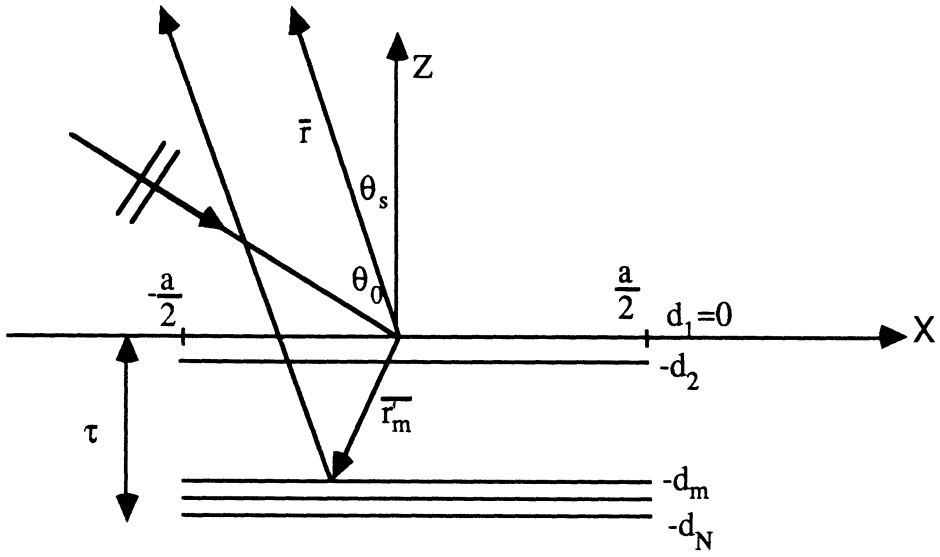

Figure 4: The geometry of scattering of a plane wave from a finite N-layer combined-sheet.

If the induced electric and magnetic currents in the m^{th} sheet are denoted by $\mathbf{J}_m$ and $\mathbf{J}_m^*$ then the scattered field can be attributed to the electric and magnetic Hertz vector potentials as given in (6) and have the following form:

$$\mathbf{\Pi}(\bar{r}) = \frac{iZ_0}{4\pi k_0} \sum_{m=1}^{N} \int \mathbf{J}_m(\bar{r}') \frac{e^{ik_0|\bar{r}-\bar{r}'_m|}}{|\bar{r}-\bar{r}'_m|} ds'_m$$

$$\mathbf{\Pi}^*(\bar{r}) = \frac{iY_0}{4\pi k_0} \sum_{m=1}^{N} \int \mathbf{J}_m^*(\bar{r}') \frac{e^{ik_0|\bar{r}-\bar{r}'_m|}}{|\bar{r}-\bar{r}'_m|} ds'_m$$

where

$$\bar{r} = r(-\sin\theta_s \hat{\mathbf{x}} + \cos\theta_s \hat{\mathbf{z}}),$$

$$\bar{r}'_m = x'\hat{\mathbf{x}} + y'\hat{\mathbf{y}} - d_m\hat{\mathbf{z}}.$$

The scattered field in terms of the Hertz vector potentials can be obtained from (8). In the far zone the approximation

$$| \bar{r} - \bar{r}'_m | \approx r + \sin\theta_s x' + \cos\theta_s d_m$$

leads to

$$\mathbf{\Pi}(\bar{r}) \approx \frac{e^{ik_0 r}}{k_0 r}\frac{iZ_0}{4\pi}\int_{-a/2}^{a/2}\int_{-b/2}^{b/2}(\sum_{m=1}^{N}\mathbf{J}_m(\bar{r}')e^{ik_0\cos\theta_s d_m})e^{ik_0\sin\theta_s x'}\mathrm{d}x'\mathrm{d}y', \qquad (60)$$

$$\mathbf{\Pi}^*(\bar{r}) \approx \frac{e^{ik_0 r}}{k_0 r}\frac{iY_0}{4\pi}\int_{-a/2}^{a/2}\int_{-b/2}^{b/2}(\sum_{m=1}^{N}\mathbf{J}^*_m(\bar{r}')e^{ik_0\cos\theta_s d_m})e^{ik_0\sin\theta_s x'}\mathrm{d}x'\mathrm{d}y'. \qquad (61)$$

Using the physical optics approximation, the currents obtained for the infinite layered sheets will be substituted in expressions (60) and (61) in order to find the scattered fields.

6.1 E-polarization

For E-polarization the induced magnetic current $\mathbf{J}^{E*}$ is zero which renders $\mathbf{\Pi}^* = 0$, and upon inserting expression (46b) for $\mathbf{J}^E_m(x)$ in (60) we have

$$\mathbf{\Pi}(\bar{r}) = \hat{\mathbf{y}}\frac{e^{ik_0 r}}{k_0 r}\frac{iZ_0}{4\pi}(\sum_{m=1}^{N}\mathbf{J}^E_m e^{ik_0\cos\theta_s d_m})ab\frac{\sin X}{X} \qquad (62)$$

where, as before, $X = \frac{ka}{2}(\sin\theta_s + \sin\theta_0)$. In this case the far-field amplitude as defined by (13) has the following form:

$$\mathbf{S}_E(\theta_s,\theta_0) = \hat{\mathbf{y}}\frac{i}{4\pi}k_0^2 abZ_0(\sum_{m=1}^{N}\mathbf{J}_m e^{ik_0\cos\theta_s d_m})\frac{\sin X}{X}, \qquad (63)$$

from which the bistatic scattering cross section can be obtained as given in (15). The extinction cross section can also be obtained from the far field amplitude from

$$\sigma^{ext} = \frac{\lambda^2}{\pi} I_m[\mathbf{S}(\theta_0,\theta_0+\pi)]. \qquad (64)$$

In backscattering ($\theta_s = \theta_0$) and in the specular direction ($\theta_s = -\theta_0$) the summation term in (63) reduces to a telescopic series using equation (49a) for $\mathbf{J}_m^E$, resulting in

$$\sum_{m=1}^{N} \mathbf{J}_m^E e^{ik\cos\theta_0 d_m} = 2Y_0 \cos\theta_0 C_0^r = 2Y_0 \cos\theta_0 \Gamma_E(\theta_0), \tag{65}$$

and

$$\sigma_E(\theta_0, \theta_0) = 4\pi \frac{(ab)^2}{\lambda^2} \cos^2\theta_0 \mid \Gamma_E(\theta_0) \mid^2 \frac{\sin^2(ka\sin\theta_0)}{(ka\sin\theta_0)^2}. \tag{66}$$

The extinction cross section can also be simplified using (46b) as follows

$$\sum_{m=1}^{N} \mathbf{J}_m^E e^{-ik\cos\theta_0 d_m} = 2Y_0 \cos\theta_0 (1 - T_E(\theta)),$$

and

$$\sigma_E^{ext} = 2ab\cos\theta_0 Re[1 - T_E(\theta)]. \tag{67}$$

6.2 H-polarization

For H-polarization the Hertz vector potentials are of the form

$$\mathbf{\Pi}(\bar{r}) = \hat{\mathbf{x}} \frac{e^{ik_0 r}}{k_0 r} \frac{iZ_0}{4\pi} \left(\sum_{m=1}^{N} \mathbf{J}_m^H e^{ik_0 \cos\theta_s d_m} \right)$$

$$\mathbf{\Pi}^*(\bar{r}) = \hat{\mathbf{y}} \frac{e^{ik_0 r}}{k_0 r} \frac{iY_0}{4\pi} \left(\sum_{m=1}^{N} \mathbf{J}_m^{H*} e^{ik\cos\theta_s d_m} \right) ab \frac{sinX}{X},$$

and the scattered magnetic field is given by

$$\mathbf{H}^s = \frac{e^{ik_0 r}}{k_0 r} \mathbf{S}_H(\theta_s, \theta_0),$$

where

$$\mathbf{S}_H(\theta, \theta_0) = \hat{\mathbf{y}} \frac{i}{4\pi} k_0^2 ab \left[\sum_{m=1}^{N} (\cos\theta_s \mathbf{J}_m^H + Y_0 \mathbf{J}_m^{H*}) e^{ik_0 \cos\theta_s d_m} \right] \frac{\sin X}{X}. \tag{68}$$

The bistatic cross section can be obtained from (15) and the backscattering cross section can be simplified using expressions (56) and (57) for J_m^H and J_m^{H*}:

$$\begin{aligned}&\textstyle\sum_{m=1}^{N}(cos\theta_0 J_m^H + Y_0 J_m^{H*})e^{ik_0\cos\theta_0 d_m} = \\ &-2\cos\theta_0 \textstyle\sum_{m=1}^{N}(B_{m-1}^r - B_m^r) = -2\cos\theta_0 B_0^r = -2\cos\theta_0\Gamma_H(\theta_0),\end{aligned} \tag{69}$$

which leads to

$$\sigma_H(\theta_0,\theta_0) = 4\pi\frac{(ab)^2}{\lambda^2}\cos^2\theta_0 \mid \Gamma_H(\theta_0) \mid^2 \frac{\sin^2(ka\sin\theta_0)}{(ka\sin\theta_0)^2}. \tag{70}$$

The extinction cross section also can be simplified by noting that

$$\sum_{m=1}^{N}(-\cos\theta_0 J_m^H + Y_0 J_m^{H*})e^{-ik\cos\theta_0 d_m} = 2\cos\theta_0(1 - T_H(\theta_0))$$

from which we obtain

$$\sigma_H^{ext} = 2ab\cos\theta_0 Re[1 - T_H(\theta_0)].$$

7 Numerical Results

To illustrate the difference between the VIPO and SCPO approximations we consider a homogeneous (single layer) plate of thickness $d_2 = \lambda_0/4$ with $\epsilon_2 = \epsilon_1 = 3 + i0.1$. For an E-polarized plane wave incident at 30 degrees, the amplitude and phase of $\mathbf{S}^{VIPO}/\mathbf{S}^{SCPO}$ are given in Figs. 5 and 6, and these show that the difference increases away from the specular and backscattering directions. At a fixed scattering angle, the difference increases with the electrical thickness of the plate up to the first resonance and then decreases. To test their accuracy the two approximations have been compared with the results of a moment method solution

of the volume integral equation as given in Appendix A. The numerical code is a two-dimensional one which was extended to three dimensions by assuming that the induced currents are independent of the y coordinate. Since the dielectric constant of most vegetation materials is high, it is necessary to have the cell sizes very small, and one consequence of this is the need to compute the matrix elements extremely accurately, especially for H polarization. For a $2\lambda_0$ square plate formed from the above-mentioned layer and illuminated by an E-polarized plane wave at normal incidence, the two approximations are compared with the moment method solution in Fig. 7, and the superiority of VIPO is clear.

In the case of a thin plate the two approximations are indistinguishable. This is illustrated in Fig. 8 showing the VIPO expression (14) and the moment method solution for a $2\lambda_0$ square plate of thickness $d_2 = \lambda_0/50$ for E polarization. The plate is a homogeneous one having $\epsilon = 13 + i12$ corresponding to the average permittivity at 35 GHz in Table 1. The SCPO expression (18) yields the same results, as does a two-layer model having the permittivities listed in Table 1. The analogous data for H polarization are given in Fig. 9, and over a wide range of scattering angles, the approximate and moment method solutions are in excellent agreement.

As the frequency and, hence, the electrical thickness of the plate increase, the superiority of the VIPO approximation becomes apparent and, in addition, it becomes necessary to take the layering of the plate into account. In Figs. 10 and 11 the simulated frequency is 140 GHz, but to keep the moment method calculations

tractable, the plate has been reduced in size to $1.4\lambda_0$ by $2\lambda_0$. The curves shown are for a two-layer plate having $d_2 = 2d_1 = 0.5mm$ with $\epsilon_1 = 5+i4$ and $\epsilon_2 = 2+i1$, and for a single layer having the average permittivity $\epsilon_{avg} = 3.5 + i2.5$ (see Table 1). Since the accuracy of the physical optics approximation increases with the plate size, the agreement between the two-layer VIPO approximation and the moment method solution is remarkably good, and significantly better than if a single layer had been used.

To test the validity of the combined-sheet multilayer model, the reflection coefficient Γ was computed using (44) for a dielectric slab with a uniform dielectric profile and then compared with the exact solution given by (5) for the reflection coefficient of a uniform dielectric slab. Figure 12, which depicts the amplitude of the reflection coefficient as a function of slab thickness, contains three plots: (a)$\mid \Gamma \mid$ for the uniform slab (exact solution), (b)$\mid \Gamma \mid$ for a multilayer slab (combined sheet model) composed of identical layers each $\lambda/100$-thick, and (c) $\mid \Gamma \mid$ of a single-sheet slab, included here for comparison. Figure 13 shows similar plots for the phase of the reflection coefficient. The results indicate that the overall agreement between (a) and (b) is excellent, and that the single sheet model can successfully predict the reflection coefficient if the layer thickness is less than $\lambda/50(\sim \frac{\lambda}{15\sqrt{|\epsilon|}})$.

Now the combined-sheet multilayer model when used in conjunction with physical optics will be checked against the method of moments. Figure 14 shows a plot of the bistatic scattering cross section of a $2\lambda \times 2\lambda$ dielectric slab with thickness $\lambda/100$ computed using the physical optics expression (63) and a second plot

computed according to the moment method, both for E polarization at 35 GHz. Similar plots are shown in Fig. 15 using expression (68) for H polarization. The result of combined-sheet model are in very good agreement with the numerical data (moment method) over a wide range of the scattering angle θ_s.

In order to check the formulation for thick dielectric slabs while keeping the numerical code tractable, our next example is a $1\lambda \times 2\lambda$ dielectric slab whose thickness is $\lambda/10$. Figures 16 and 17 compare the bistatic radar cross section of the thick slab at 35 GHz computed using a 5-layer and a 1-layer combined-sheet model with physical optics approximation with the numerical data for E- and H-polarization, respectively. Keeping in mind that the accuracy of the physical optics approximation improves as the width of the slab increases, the good agreement of the 5-layer sheet with the numerical data around the specular region ($| \theta_s | \leq \pi/4$ in this case) provides good support for the model proposed in this paper.

8 Conclusions

A typical leaf has at least two dielectric layers whose cells have differing water content, and this produces a nonuniform dielectric profile which can now affect the scattering. At microwave frequencies where the leaf is no more than (about) $\lambda_0/50$ in thickness, the nonuniformity is not important, and as shown by Senior et al [1987] the leaf can be modeled as a resistive sheet using an average value for the permittivity. If the physical optics approximation is then applied, the resulting scattering is attributed to a surface current, and this method is equivalent to the

SCPO approximation. At higher frequencies, however, the thickness and structure of a leaf are more significant. At 100 GHz and above a leaf is a considerable fraction of a wavelength in thickness, and in spite of the reduced sensitivity to water content, the nonuniformity affects the scattering.

For a two-layer model of a leaf, the SCPO approximation has been compared with the volume integral (VIPO) approximation. When the leaf is thin the two approximations are identical and in good agreement with data obtained from a moment method solution of the integral equation, but as the electrical thickness increases, the two approximations diverge in all directions except the specular and (for E polarization) backscattering ones. Although the VIPO approximation is more complicated, its accuracy is greater, and the agreement with the moment method data is better using a two-layer model than when a single layer of average permittivity is employed.

For most practical purposes it would appear that VIPO in conjunction with an accurate dielectric profile of a leaf provides an adequate approximation to the scattering at millimeter wavelengths. As our knowledge of the profile increases, it may be desirable to use a multi-layer model which could even simulate a continuous, nonuniform profile. We also note that at frequencies for which the leaf thickness is comparable to $\lambda_m/2$ where λ_m is the (average) wavelength in the leaf, the scattering is greatly reduced at some angle of incidence, and because the permittivity is complex, there is actually a range of angles for which this is true. Since the reduction is accompanied by an increase in the field transmitted through the leaf,

this could provide a means for penetration through a vegetation canopy.

Acknowledgement

This work was supported by the U.S. Army Research Office under contract DAAG 29-85-k-0220.

References

[1] Le Vine, D.M., A. Snyder, R.H. Lang, and H.G. Garter, Scattering from thin dielectric disks, *IEEE Trans. Antennas Propag.*, 33, 1410-1413, 1985.

[2] Sarabandi, K., T.B.A. Senior, and F.T. Ulaby, Effect of curvature on the backscattering from a leaf, *J. Electromag. Waves and Applics.*, 2, 653-670, 1988.

[3] Senior, T.B.A., K. Sarabandi, and F.T. Ulaby, Measuring and modeling the backscattering cross section of a leaf, *Radio Sci.*, 22, 1109-1116, 1987.

[4] Senior, T.B.A., and J.L. Volakis, Sheet simulation of a thin dielectric layer, *Radio Sci.*, 22, 1261-1272, 1987.

[5] Willis, T.M., H. Weil, and D.M. Le Vine, Applicability of physical optics thin plate scattering formulas for remote sensing, *IEEE Trans. Geosci. Remote Sensing*, 26, 153-160, 1988.

[6] Richmond, J.H., Scattering by dielectric a cylinder of arbitrary cross-section shape, *IEEE Trans. Antennas Propag.*, 13, 334-341, May 1965.

[7] —, TE-wave scattering by dielectric a cylinder of arbitrary cross-section shape, *IEEE Trans. Antennas Propag.*, 14, 460-464, July 1966.

[8] Harrington, R.F., *Field Computation by Moment Methods.* New York: Macmillan, 1968.

[9] Hill, S.C., D.C. Chritensen, and C.H. Durney, Power disposition patterns in magnetically-induced hyperthermia: A two-dimensional low-frequency numerical analysis, *Int. J. Radiat. Oncol. Biol. Phys.* 1983.

[10] Langan, D.K. and D.R. Wilton, Numerical solution of TE scattering by inhomogeneous two-dimensional composite dielectric/metallic bodies of arbitrary cross section, *Abstracts of 1986 Nat. Radio Sci. Meet.*, Philadelphia, PA, June 1986.

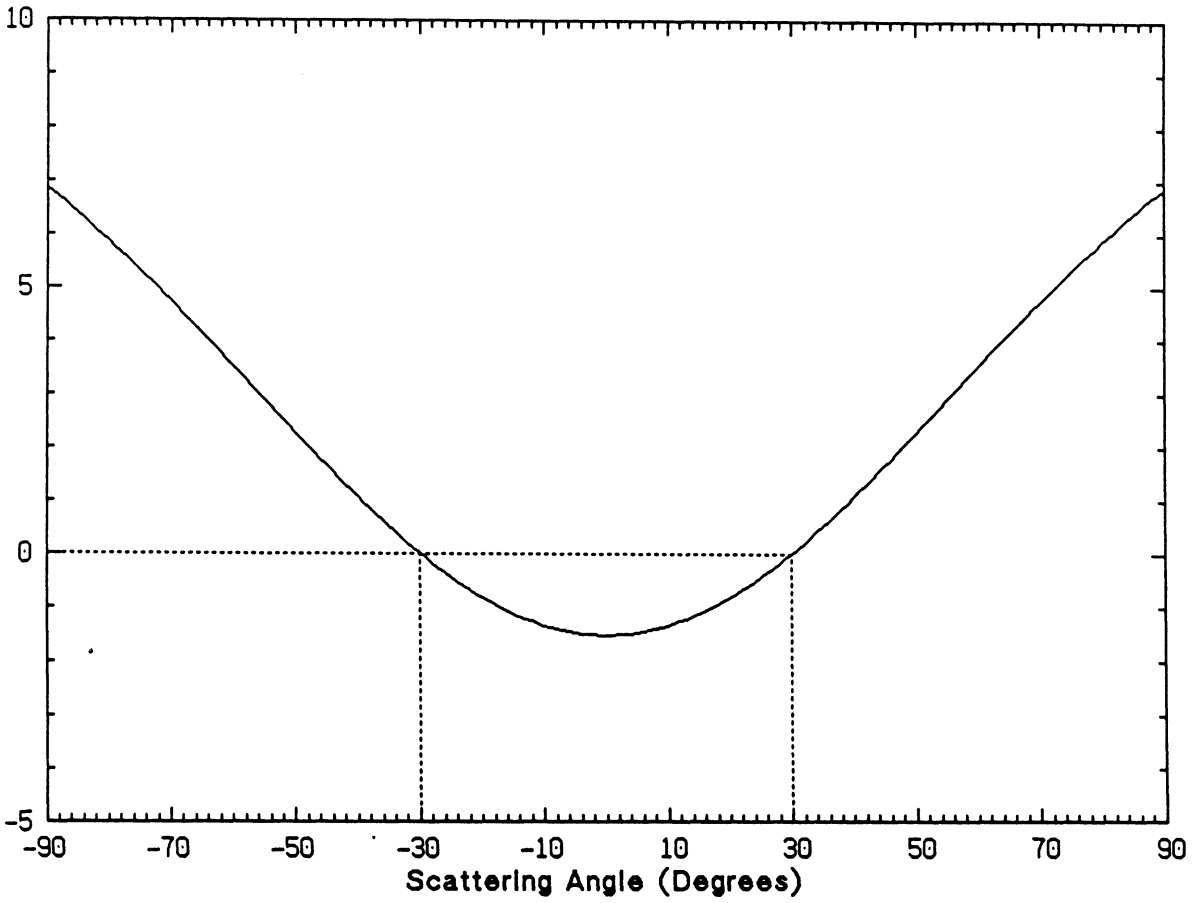

Figure 5: Amplitude of the ratio of the bistatic far field amplitude of VIPO to SCPO for E polarization of a dielectric plate with $d_2 = \lambda_0/4$ and $\epsilon_1 = \epsilon_2 = 3 + i0.1$ at $\theta_0 = 30$ degrees.

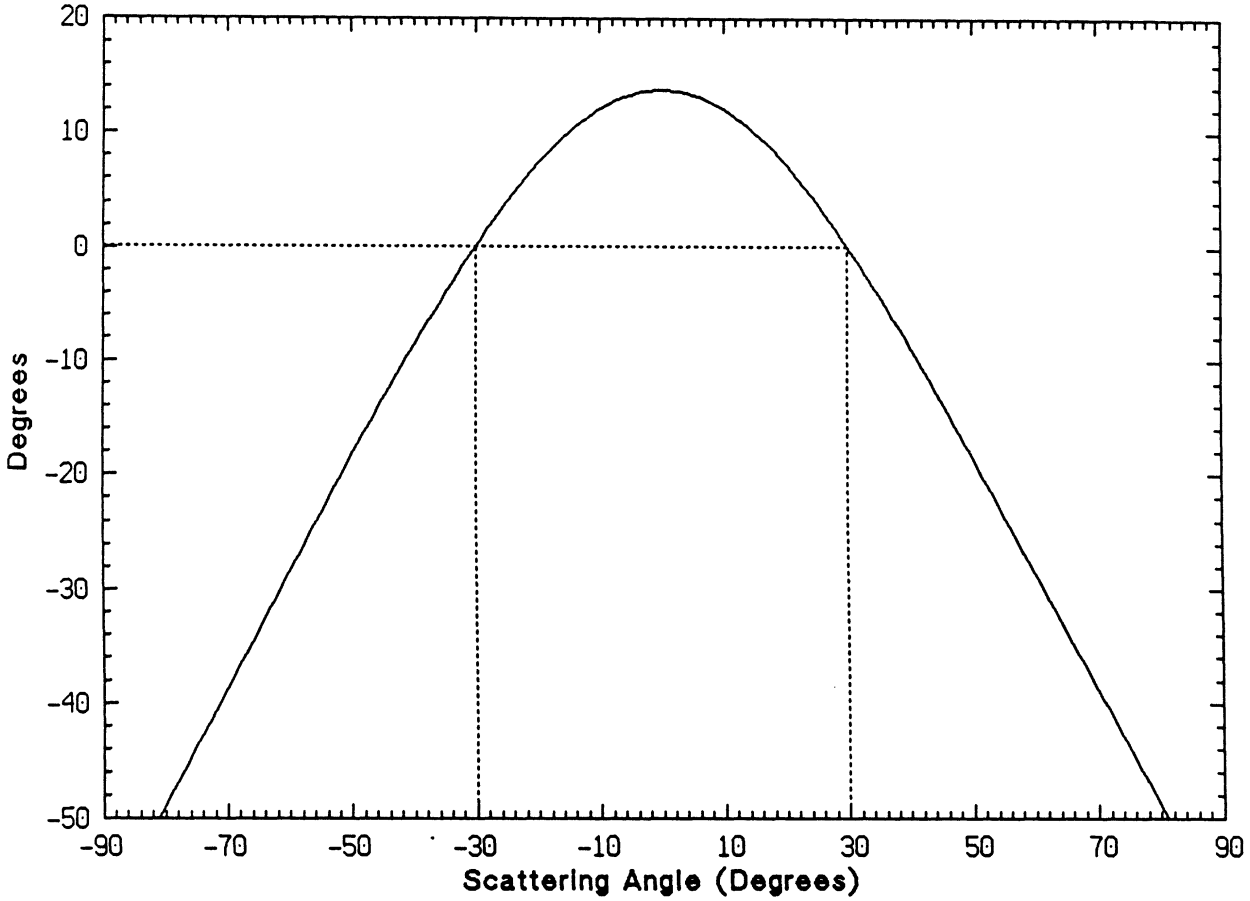

Figure 6: Phase of the ratio of the bistatic far field amplitude of VIPO to SCPO for E polarization of a dielectric plate with $d_2 = \lambda_0/4$ and $\epsilon_1 = \epsilon_2 = 3 + i0.1$ at $\theta_0 = 30$ degrees.

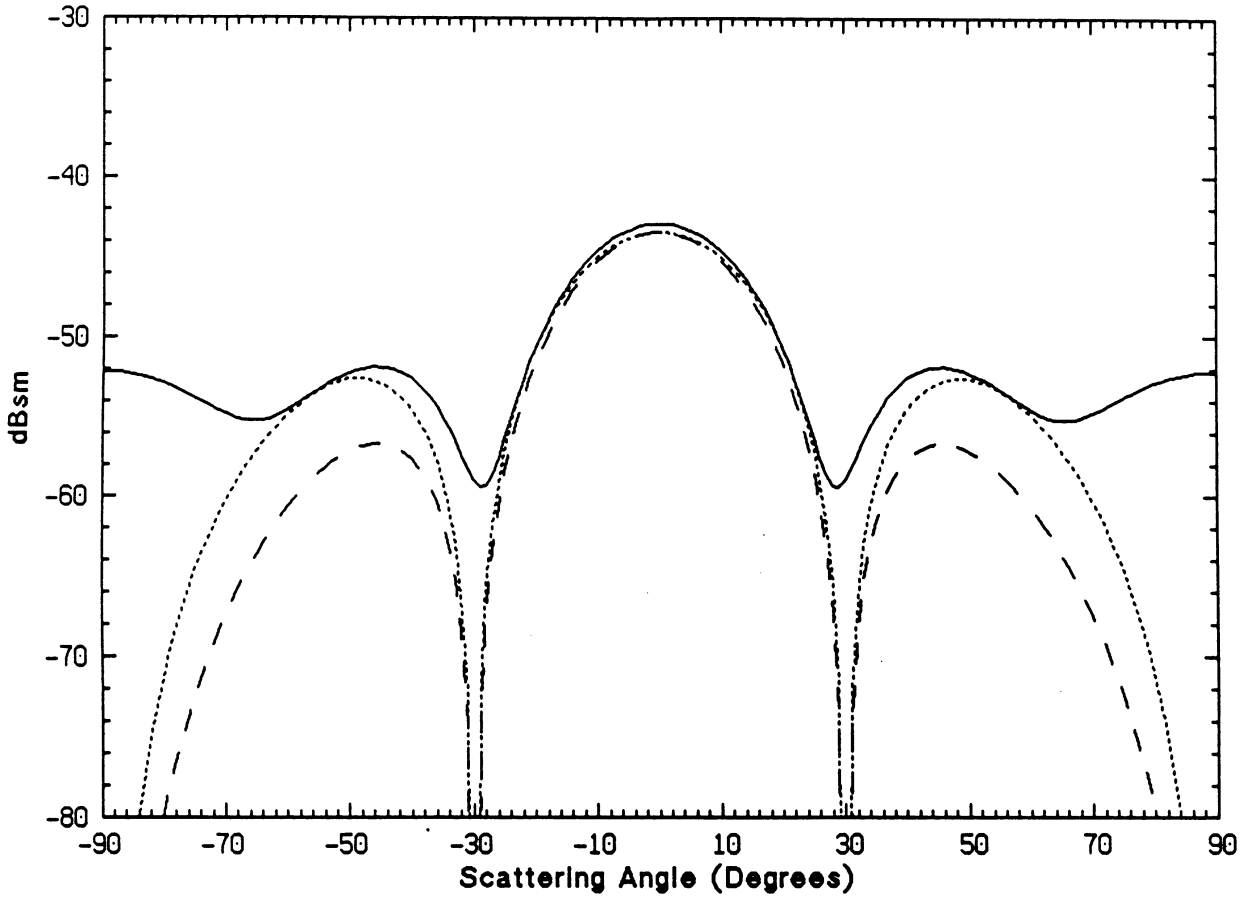

Figure 7: The bistatic cross section of a $2\lambda_0 \times 2\lambda_0$ plate for E polarization with $d_2 = \lambda_0/4$ and $\epsilon_1 = \epsilon_2 = 3 + i0.1$ at normal incidence: (——) moment method solution, (- - -) VIPO, (– –) SCPO.

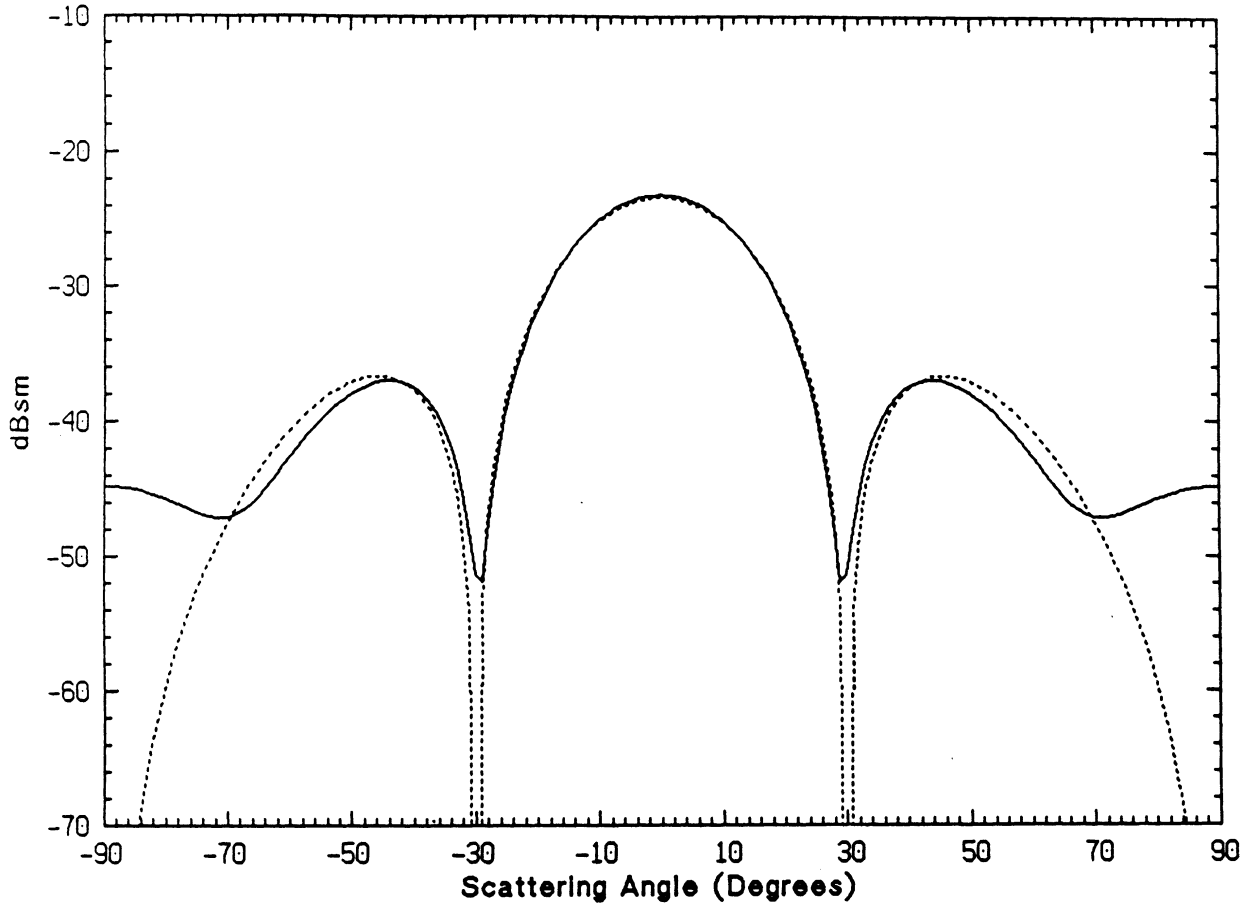

Figure 8: The bistatic cross section area of a $2\lambda_0 \times 2\lambda_0$ plate for E polarization with $d_2 = \lambda_0/50$ and $\epsilon_{avg} = 13 + i12$ at normal incidence: (——) moment method solution, (- - -) VIPO or SCPO.

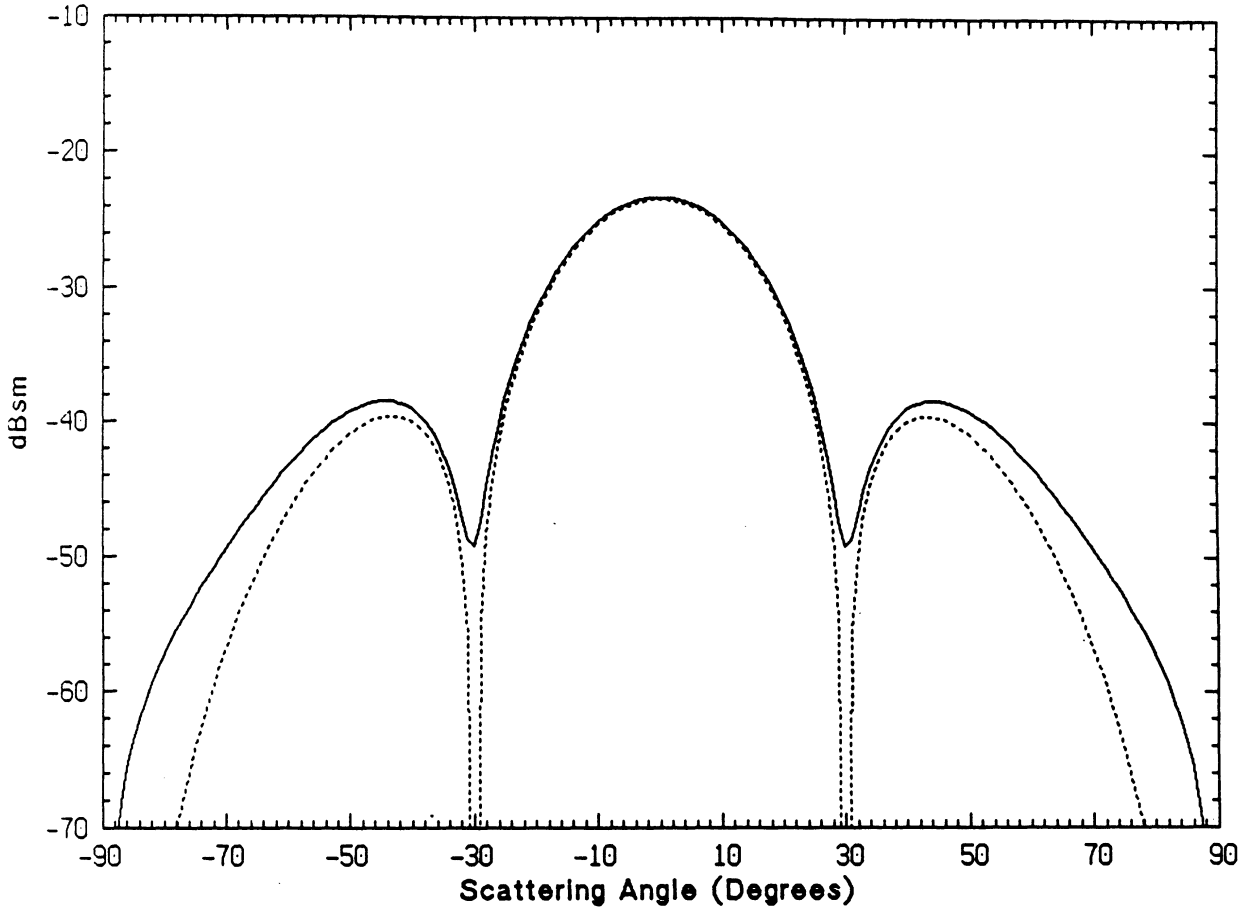

Figure 9: The bistatic cross section of a $2\lambda_0 \times 2\lambda_0$ plate for H polarization with $d_2 = \lambda_0/50$ and $\epsilon_{avg} = 13 + i12$ at normal incidence: (——) moment method solution, (- - -) VIPO or SCPO.

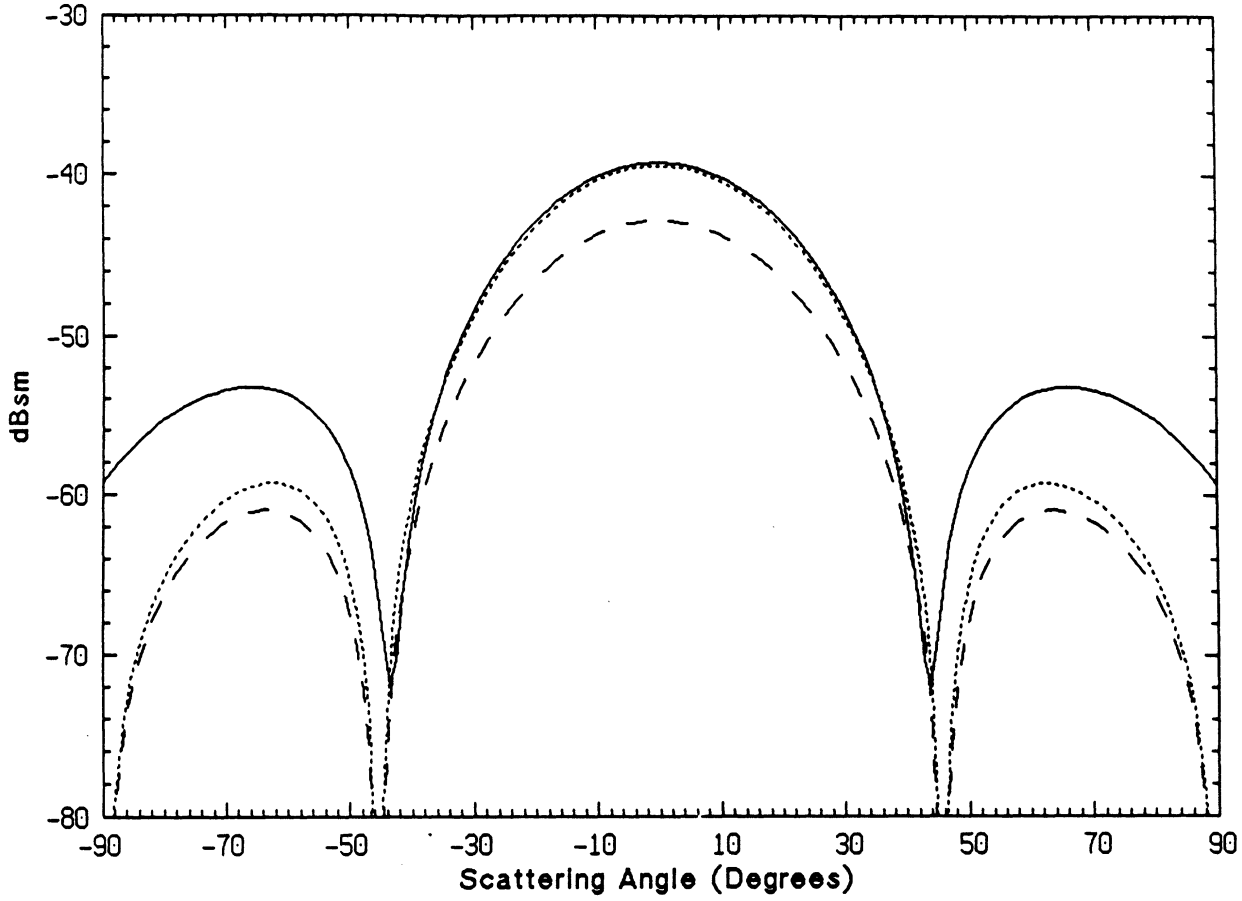

Figure 11: The bistatic cross section area of a $1.4\lambda_0 \times 2\lambda_0$ plate for H polarization with $d_2 = 2d_1 = 0.5mm$ and f =140 GHz at normal incidence: (——) moment method solution with $\epsilon_1 = 5 + i4$, $\epsilon_2 = 2 + i1$, (- - -) VIPO with $\epsilon_1 = 5 + i4$ $\epsilon_2 = 2 + i1$, (– –) VIPO with $\epsilon_2 = \epsilon_1 = 3.5 + i2.5$.

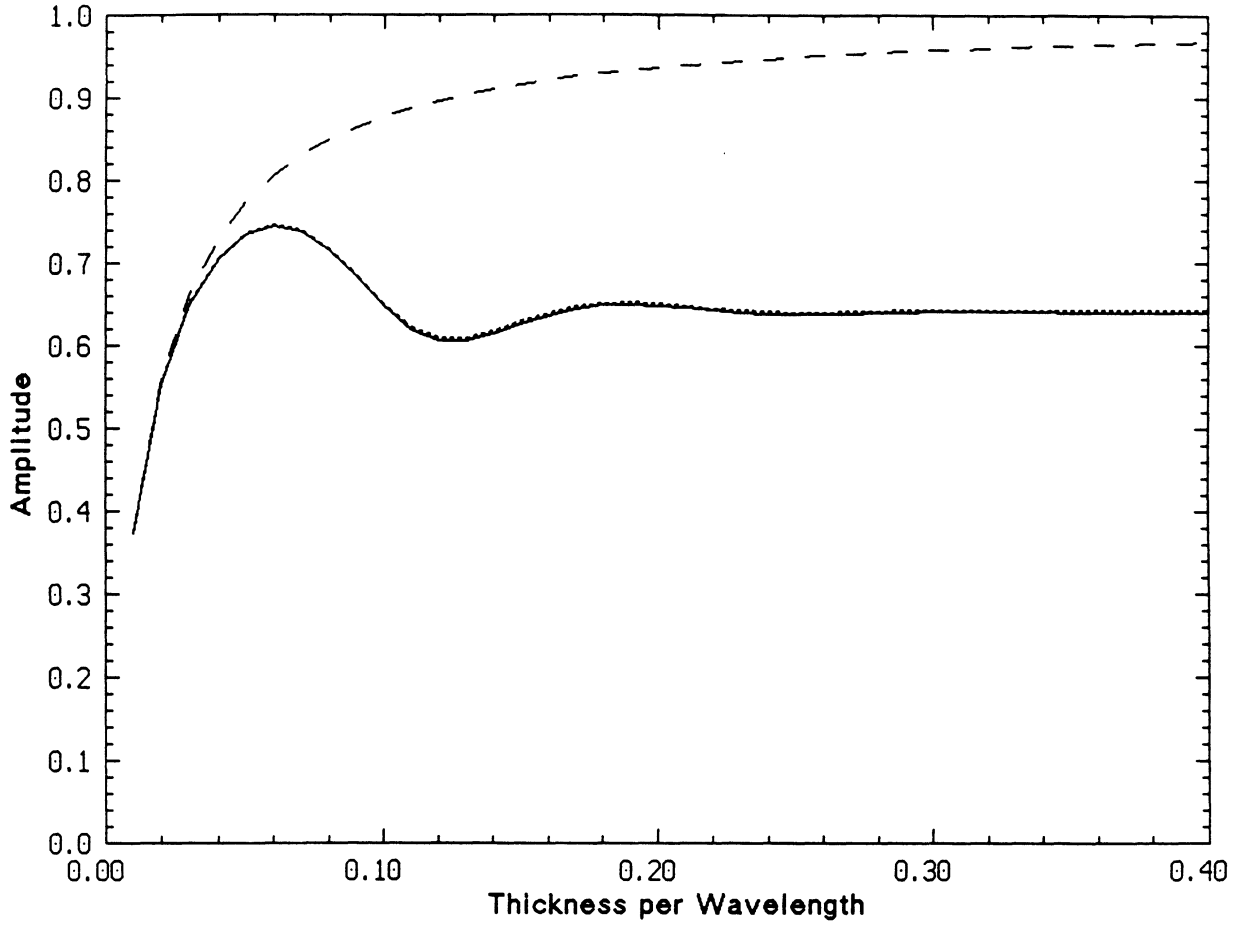

Figure 12: Amplitude of the reflection coefficient at f=35GHz, $\theta_0 = 0$,and $\epsilon = 13 + i12$ as a function of thickness: (——) exact solution, (- - -) N-layered combined-sheet model $\Delta = \lambda/100$, (– –) single-sheet $\Delta = \tau$.

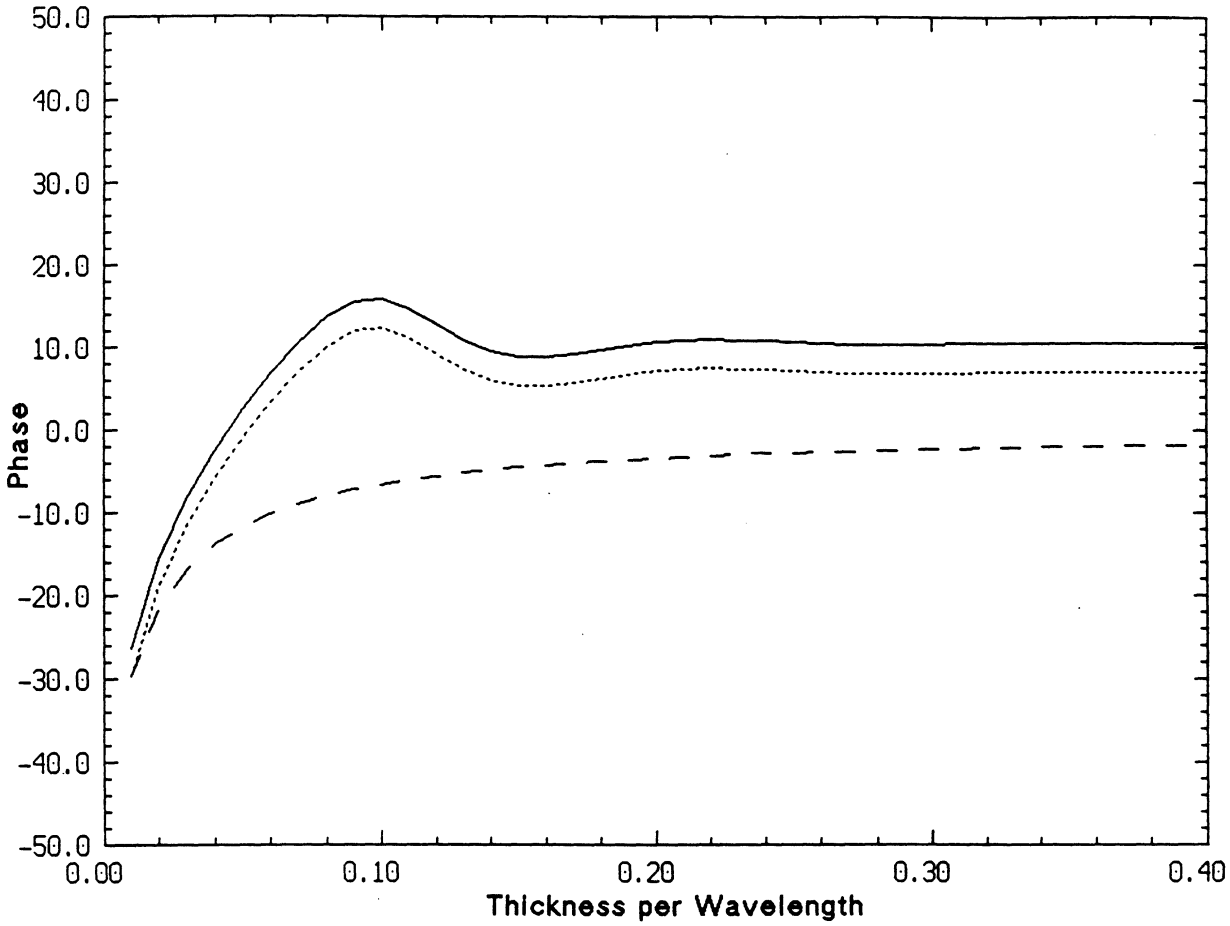

Figure 13: Phase of the reflection coefficient at f=35GHz, $\theta_0 = 0$,and $\epsilon = 13 + i12$ as a function of thickness: (——) exact solution, (- - -) N-layered combined-sheet model $\Delta = \lambda/100$, (– –) single-sheet $\Delta = \tau$.

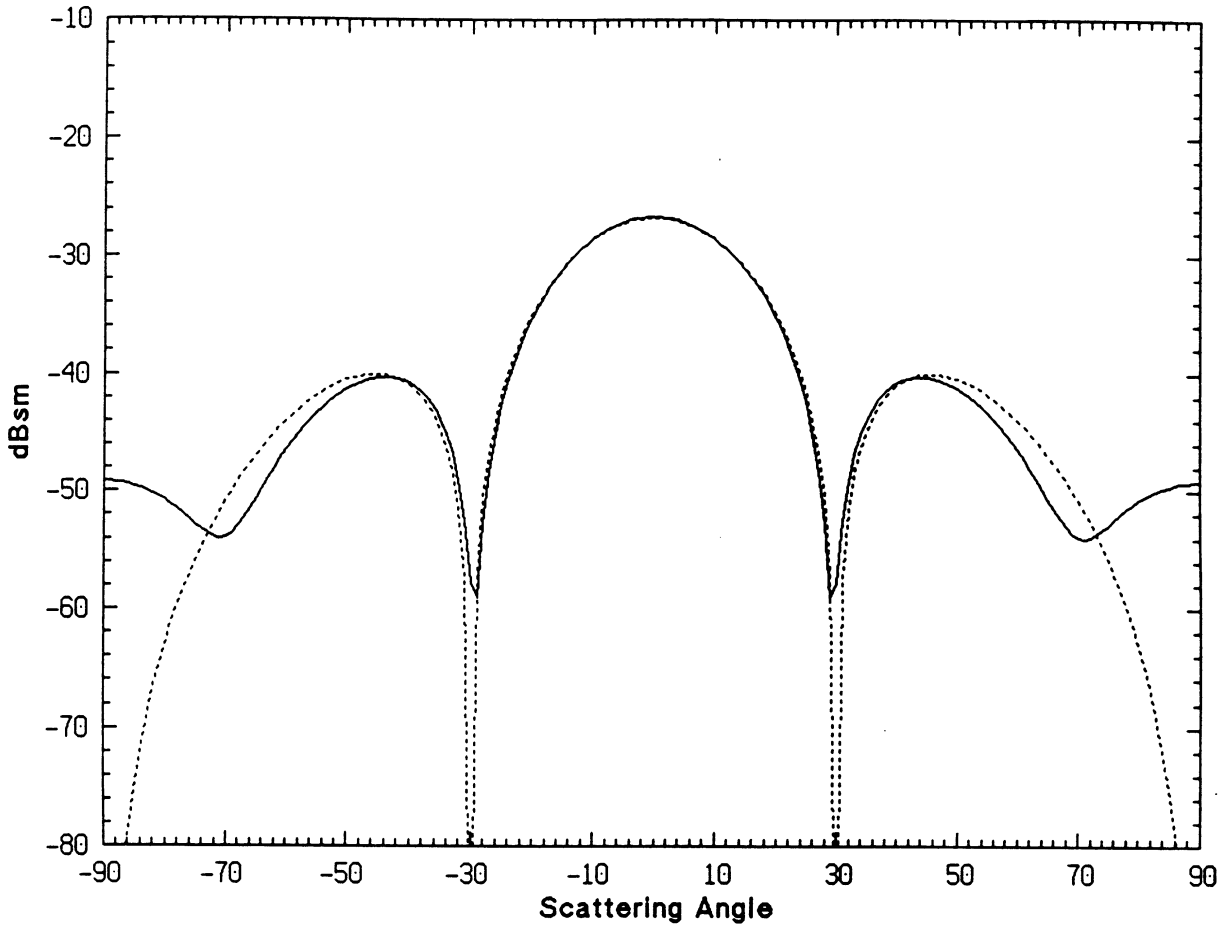

Figure 14: Bistatic scattering cross section of a $2\lambda \times 2\lambda$ dielectric plate with $\tau = \lambda/100$ for E-polarization at f=35GHz, $\theta_0 = 0$, and $\epsilon = 13 + i12$ as function of scattering angle: (——) moment method, (- - -) single-layered combined-sheet model.

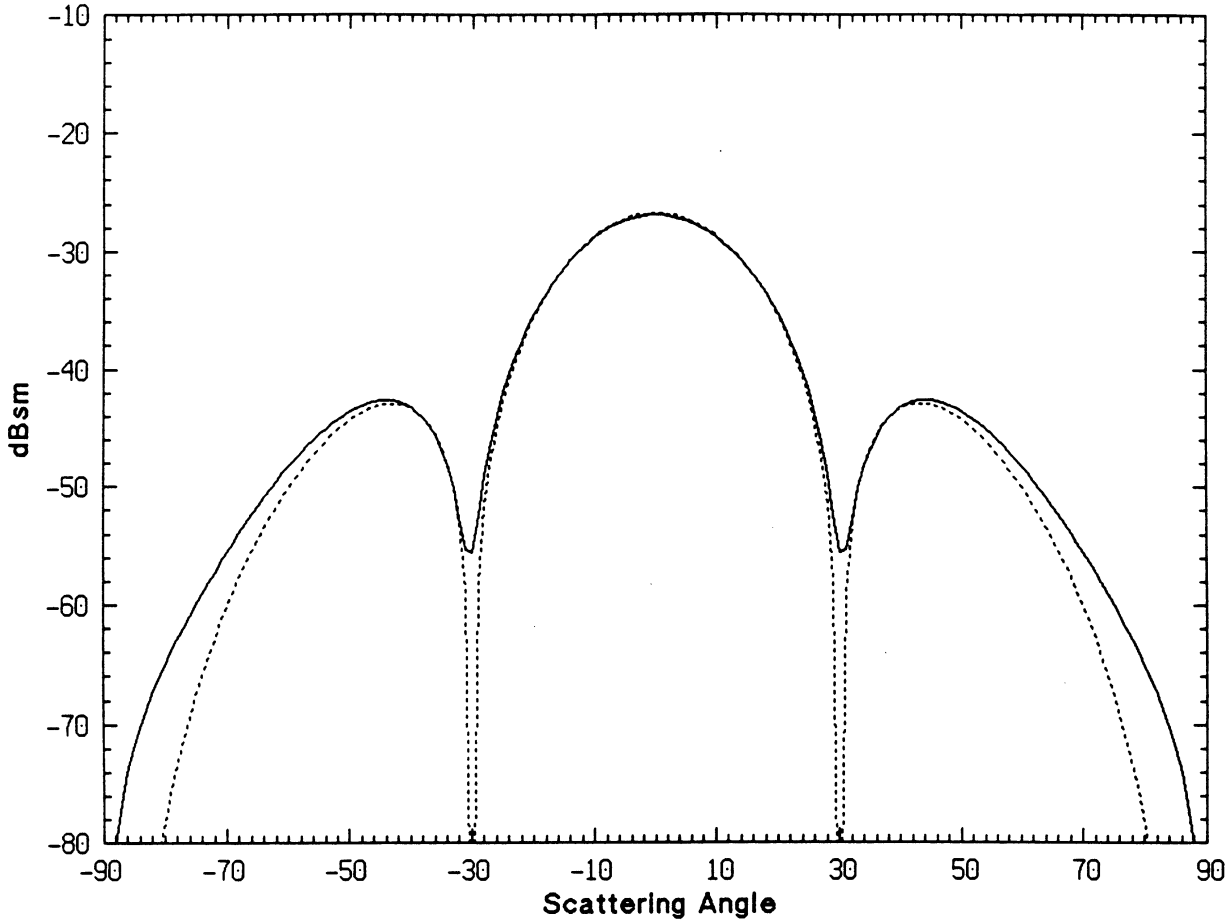

Figure 15: Bistatic scattering cross section of a $2\lambda \times 2\lambda$ dielectric plate with $\tau = \lambda/100$ for H-polarization at f=35GHz, $\theta_0 = 0$, and $\epsilon = 13 + i12$ as function of scattering angle: (——) moment method, (- - -) single-layered combined-sheet model.

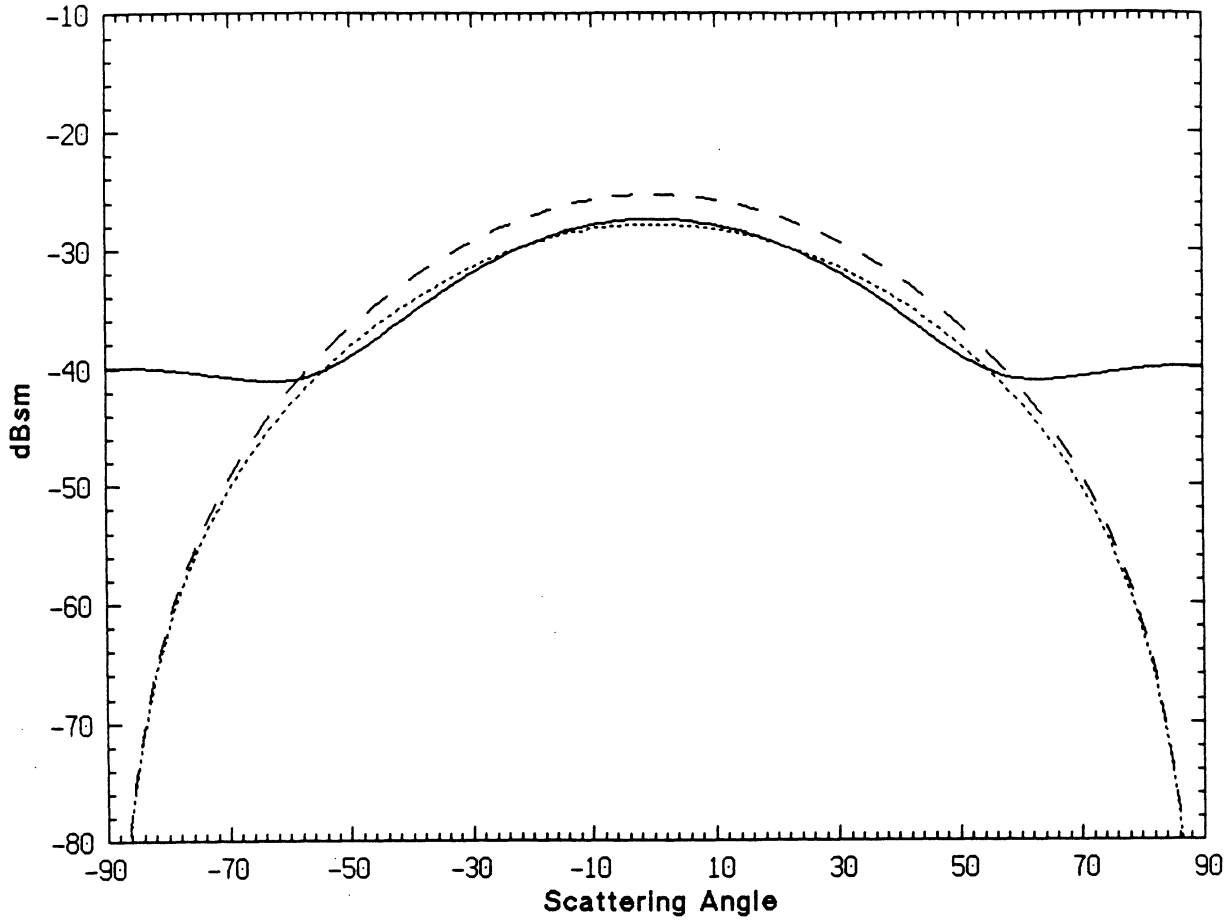

Figure 16: Bistatic scattering cross section of a $1\lambda \times 2\lambda$ dielectric plate with $\tau = \lambda/10$ for E-polarization at f=35GHz, $\theta_0 = 0$, and $\epsilon = 13 + i12$ as function of scattering angle: (——) moment method, (- - -) 5-layered combined-sheet model, (– –) single-sheet.

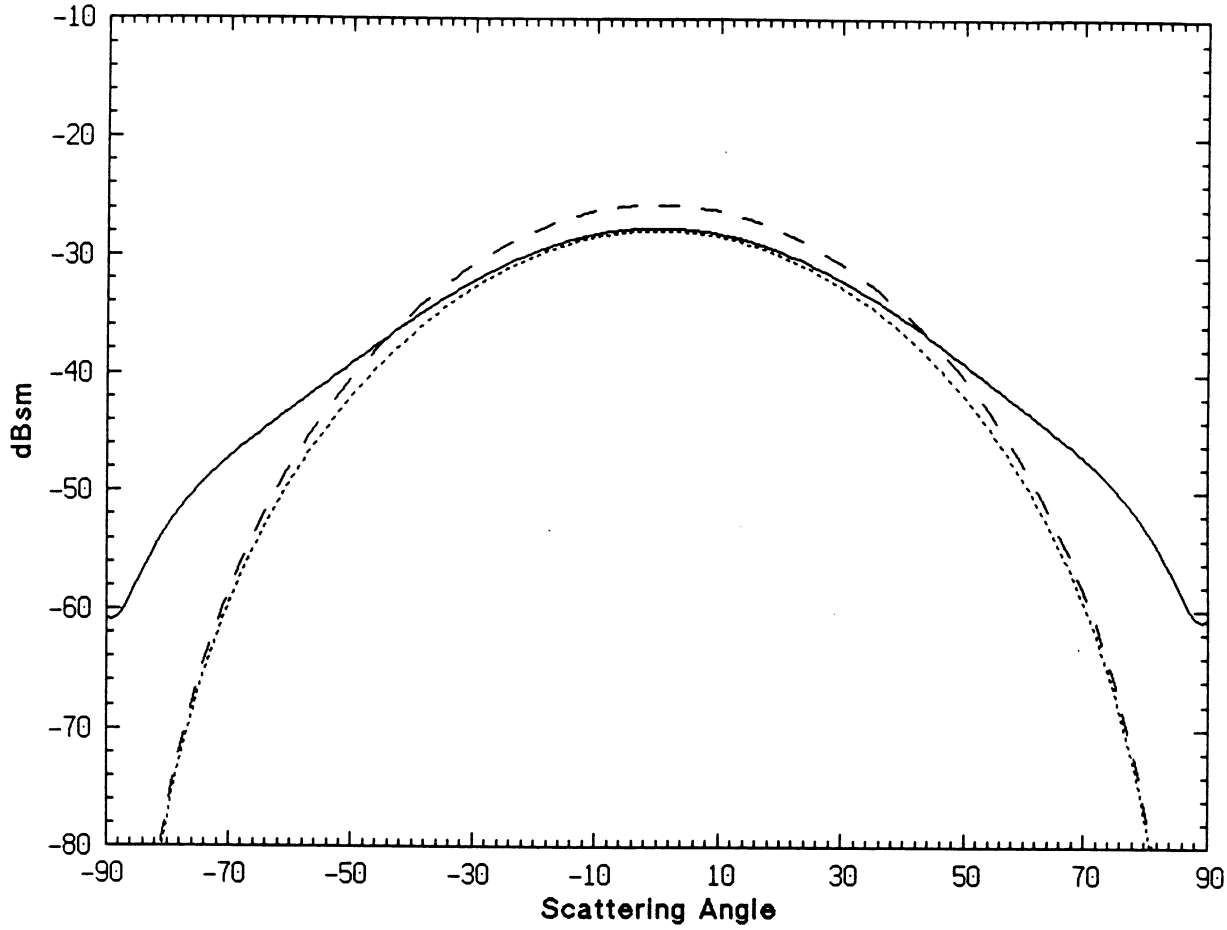

Figure 17: Bistatic scattering cross section of a $1\lambda \times 2\lambda$ dielectric plate with $\tau = \lambda/10$ for H-polarization at f=35GHz, $\theta_0 = 0$, and $\epsilon = 13 + i12$ as function of scattering angle: (——) moment method, (- - -) 5-layered combined-sheet model, (– –) single-sheet.

Appendix A
Two Dimensional Scattering by Cylindrical Structures with High Refractive Index

1 Introduction

A numerical solution for the problem of electromagnetic scattering by a lossy inhomogeneous cylinder of arbitrary cross section is discussed. An integro-differential equation is employed to obtain the moment method solution using pulse expansion function and point matching technique. In this method the cross section of the scatterer is partioned into small cells over which the dielectric constant and the unknown field quantities can be assumed constant. Then the integral equation is cast into a linear system of equation that can be solved by various numerical methods. This technique was developed many years ago [Richmond 1965 & 1966; Harrington 1968] and has been applied successfully for cylinders with relatively small refractive indeces. The integral equation operator given by Harrington is such that in the TE case (the electric field vector perpendicular to the axis of the cylinder) in using pulse expansion functions numerical computation does not converge to the exact solution. To obtain accurate results in this case more complicated expansion functions such as linear expansion function [Hill et al. 1983] or rooftop expansion function [Langan & Willton 1986] must be used. To avoid using complicated expansion functions and to reduce computation time, we use an integral equation where the pulse functions are in the domain of the integro-differential operator for both TE and TM (the magnetic field vector perpendicular to the axis of the cylinder) cases.

It is known, in principle, that the accuracy of the solution is proportional to the dimension of the cells relative to the wavelength, which in turn is governed by the dielectric constant of cylinder material. The accepted criterion for the cell dimension is $d < 0.1\lambda_0/\sqrt{|\epsilon_r|}$ where λ_0 is the wavelength in free space and ϵ_r is the relative permittivity of the dielectric material.

Biological tissues usually have high percentage of water content, as a result of which their dielectric constant is very high and lossy. In application of the moment method to biological scatterers, the cell size must be chosen very small compared to the free-space wavelength. Since the argument of Green's function becomes very small, contribution of self-cell and adjacent cells must be evaluated very carefully to avoid anomalous errors.

Unlike the TE case in which approximations on deforming the cell shape can culminate in substantial error, the solution for the TM case is not very sensitive the the shape of the cells. When using the moment method with traditional impedance matrix elements [Richmond 1965 & 1966], as the dimension of the cells gets very small, the technique becomes vulnerable to two sources of error: (1) error due to deformation of cell shapes to circles of equivalent area, and (2) errors associated with the evaluation of mutual impedance of the adjacent cells. The effect of the latter again is much more significant in the TE case than the TM case because of higher degree of singularity in the kernel of the integral equation.

For a scatterer with fixed dimensions, as the dielectric constant increases the impedance matrix becomes larger and so does the error due to matrix inversion. This problem is unavoidable in general but the error can be lowered by using

double-precision variables in the numerical code.

2 Formulation

Let us consider an inhomogeneous infinite cylinder with arbitrary cross section S as illustrated in Fig. 1. The axis of the cylinder is parallel to the z axis and the surrounding medium is assumed to be free space. Let relative the permittivity of the cylinder be $\epsilon_r(x,y)$ and its relative permeability be unity ($\mu_r = 1$). Suppose the electric field in the absence of the cylinder (the incident field) is not dependent upon z and is represented by $\mathbf{E}^i(x,y)$. Further assume that the incident field is time-harmonic of the form $e^{-i\omega t}$, which will be suppressed throughout. The cylinder perturbs the incident field and the difference between the perturbed (total) and incident field is known as the scattered field; thus,

$$\mathbf{E}^t(\bar{\rho}) = \mathbf{E}^i(\bar{\rho}) + \mathbf{E}^s(\bar{\rho}), \tag{A1}$$

where $\bar{\rho}$ is the position vector in cylindrical coordinate. From Maxwell's equations it can be shown that a volumetric current density of the form

$$\mathbf{J}(\bar{\rho}) = -ik_0 Y_0[\epsilon_r(\bar{\rho}) - 1]\mathbf{E}^t(\bar{\rho}), \qquad \bar{\rho} \in S, \tag{A2}$$

known as the polarization current in free space, can replace the cylinder to reproduce the scattered field. Therefore the scattered field, can be obtained from:

$$\mathbf{E}^s(\bar{\rho}) = -ik_0 Z_0 \int_s \mathbf{J}(\bar{\rho'}) \cdot \bar{\bar{\Gamma}}(\bar{\rho}, \bar{\rho'}) \mathrm{d}s', \tag{A3}$$

where $\bar{\bar{\Gamma}}(\bar{\rho}, \bar{\rho'})$ is the two-dimensional dyadic Green's function and is given by

$$\bar{\bar{\Gamma}}(\bar{\rho}, \bar{\rho'}) = -\frac{i}{4}[\bar{\bar{I}} + \frac{\nabla\nabla}{k_0^2}]H_0^{(1)}(k_0 \mid \bar{\rho} - \bar{\rho'} \mid).$$

Here, $H_0^{(1)}$ is the Hankel function of the first kind and zeroth-order and $\bar{\rho}'$ represents the source position in cylindrical coordinates. Using (A1), (A2),and (A3) an integral equation for the unknown polarization current can be obtained,

$$\mathbf{J}(\bar{\rho}) = -ik_0Y_0[\epsilon_r(\bar{\rho}) - 1]\{\mathbf{E}^i(\bar{\rho}) - ik_0Z_0\int_s \mathbf{J}(\bar{\rho}')\cdot\bar{\bar{\Gamma}}(\bar{\rho},\bar{\rho}')\mathrm{d}s'\}.$$

If the incident field has a uniform polarization, then the problem may be decoupled into TM and TE problems. For the TM case the incident, scattered, and hence, the polarization current have only z components and the integral equation is

$$\begin{aligned} J_z(x,y) = \; & -ik_0Y_0[\epsilon_r(x,y) - 1]E_z^i(x,y) + i\tfrac{k_0^2}{4}[\epsilon_r(x,y) - 1] \\ & \textstyle\int_s J_z(x',y')H_0^{(1)}(k_0 \mid \vec{\rho} - \vec{\rho}' \mid)\mathrm{d}x'\mathrm{d}y'\}. \end{aligned} \tag{A4}$$

In the TE case both x and y components of the polarization current are induced and they satisfy the following coupled integro-differential equations

$$\begin{aligned} J_x(x,y) = \; & -ik_0Y_0[\epsilon_r(x,y) - 1]E_x^i(x,y) + \tfrac{i}{4}[\epsilon_r(x,y) - 1] \\ & \cdot\{(\tfrac{\partial^2}{\partial x^2} + k_0^2)\textstyle\int_s J_x(x',y')H_0^{(1)}(k_0 \mid \vec{\rho} - \vec{\rho}' \mid)\mathrm{d}x'\mathrm{d}y' \\ & +\tfrac{\partial^2}{\partial x\partial y}\textstyle\int_s J_y(x',y')H_0^{(1)}(k_0 \mid \vec{\rho} - \vec{\rho}' \mid)\mathrm{d}x'\mathrm{d}y'\} \\ J_y(x,y) = \; & -ik_0Y_0[\epsilon_r(x,y) - 1]E_y^i(x,y) + \tfrac{i}{4}[\epsilon_r(x,y) - 1] \\ & \cdot\{\tfrac{\partial^2}{\partial x\partial y}\textstyle\int_s J_x(x',y')H_0^{(1)}(k_0 \mid \vec{\rho} - \vec{\rho}' \mid)\mathrm{d}x'\mathrm{d}y' \\ & +(\tfrac{\partial^2}{\partial y^2} + k_0^2)\textstyle\int_s J_y(x',y')H_0^{(1)}(k_0 \mid \vec{\rho} - \vec{\rho}' \mid)\mathrm{d}x'\mathrm{d}y'\} \end{aligned} \tag{A5}$$

The resultant integro-differential operators obtained for the polarization current do not impose any restriction on the functional form of the current, in particular pulse function is in the domain of the operators. It should be noted here that the kernel of the integral equation (Green's function) for the TE case is more singular $(\frac{1}{\rho^2})$ than for the TM case $(\ln(\rho))$.

There is no known solution for these integral equations in general, but their forms are amenable to numerical solution.

3 Numerical Analysis

An approximate numerical solution for the integral equations that were developed in the previous Section is given using the method of moment in conjunction with the pulse expansion function and the point-matching technique. The cross section of the scatterer is divided into N rectangular cells that are small enough so that the polarization current and relative permittivity can be assumed to be constant. The unknown current can be approximated by

$$J_p(x,y) = \sum_{m=1}^{N} J_m P(x - x_m, y - y_m), \quad p = x, y, \text{ or } z \tag{A6}$$

where J_m are the unknown coefficients to be determined and $P(x - x_m, y - y_m)$ is the pulse function defined by

$$P(x - x_m, y - y_m) = \begin{cases} 1 & \mid x - x_m \mid < \frac{\Delta X_m}{2}, \quad \mid y - y_m \mid < \frac{\Delta Y_m}{2} \\ 0 & \text{otherwise} \end{cases} \tag{A7}$$

By inserting the current as expanded in (A6) into integral equations (A4) and (A5) and then setting the observation point in the center of the m$^{\text{th}}$ cell a linear set of equation is formed. In matrix notation, these linear equations can be represented by

$$[\mathcal{Z}^{TM}][\mathcal{J}_z] = [\mathcal{E}_z] \tag{A8}$$

for the TM case, where $[\mathcal{Z}^{TM}]$ is the impedance matrix, $[\mathcal{J}_z]$ is the unknown vector, and $[\mathcal{E}_z]$ is the excitation vector. Similarly for the TE case the coupled integral

equation (A5) in matrix form becomes

$$\begin{aligned} \mathcal{Z}_1^{TE}\mathcal{J}_x + \mathcal{Z}_2^{TE}\mathcal{J}_y &= \mathcal{E}_x \\ \mathcal{Z}_3^{TE}\mathcal{J}_x + \mathcal{Z}_4^{TE}\mathcal{J}_y &= \mathcal{E}_y \end{aligned} \tag{A9}$$

where as before $\mathcal{Z}_1^{TE}, \cdots, \mathcal{Z}_4^{TE}$ are $N \times N$ impedance matrices and $\mathcal{E}_x$ and $\mathcal{E}_y$ are the excitation vectors. The above coupled matrix equation can be represented by a $2N \times 2N$ matrix equation similar to (A8).

Although the variation of the polarization current and dielectric constant is assumed constant, this might not be true for the Green's function. Actually for cells close to the observation point, the Green's function varies considerably and its contribution must be evaluated more precisely. Let us denote the function representing the Green's function contribution by

$$I_n(x,y) = \int_{x_n-\frac{\Delta X_n}{2}}^{x_n+\frac{\Delta X_n}{2}} \int_{y_n-\frac{\Delta Y_n}{2}}^{y_n+\frac{\Delta Y_n}{2}} H_0^{(1)}(k_0\sqrt{(x-x')^2+(y-y')^2})\mathrm{d}x'\mathrm{d}y' \tag{A10}$$

where $1 \leq n \leq N$. If the observation point (x,y) is different from (x_n, y_n) , then the integrand in (A10) is not singular and since $\mid x' - x_n \mid \leq \frac{\Delta X_n}{2}$ and $\mid y' - y_n \mid \leq \frac{\Delta Y_n}{2}$, its Taylor series expansion may be substituted. By retaining up to the cubic terms in the expansion of Hankel function, the function (A10) is found to be:

$$\begin{aligned} I_n(x,y) = \; & \Delta X_n \Delta Y_n \{H_0^{(1)}(k_0\sqrt{(x-x_n)^2+(y-y_n)^2}) + \tfrac{(k_0\Delta X_n)^2}{24} A(x-x_n, y-y_n) + \\ & \tfrac{(k_0\Delta Y_n)^2}{24} B(x-x_n, y-y_n)\}, \end{aligned} \tag{A11}$$

where

$$A(x-x_n, y-y_n) = A(r_n, \theta_n) = -H_0^{(1)}(k_0 r_n)\cos^2\theta_n + \frac{H_1^{(1)}(k_0 r_n)}{k_0 r_n}(\cos^2\theta_n - \sin^2\theta_n), \tag{A12}$$

$$B(x-x_n, y-y_n) = B(r_n, \theta_n) = -H_0^{(1)}(k_0 r_n)\sin^2\theta_n + \frac{H_1^{(1)}(k_0 r_n)}{k_0 r_n}(\sin^2\theta_n - \cos^2\theta_n) \tag{A13}$$

with the following definition for a pair of local polar coordinates:

$$\begin{aligned} r_n &= \sqrt{(x-x_n)^2 + (y-y_n)^2} \\ \theta_n &= \arctan(\tfrac{x_n - x}{y_n - y}). \end{aligned} \tag{A14}$$

The second order derivatives of $I_n(x,y)$ are also needed for calculation of the impedance matrix elements for the TE case, and are given by

$$\begin{aligned} (\tfrac{\partial^2}{\partial x^2} + k_0^2) I_n(x,y) = \; & \Delta X_n \Delta Y_n k_0^2 \{ H_0^{(1)}(k_0 r_n)\sin^2\theta_n + \tfrac{H_1^{(1)}(k_0 r_n)}{k_0 r_n}(\cos^2\theta_n - \sin^2\theta_n) \\ & + \tfrac{\Delta X^2}{24}(\tfrac{\partial^2}{\partial x^2} + k_0^2) A(r_n, \theta_n) \tfrac{\Delta Y^2}{24}(\tfrac{\partial^2}{\partial x^2} + k_0^2) B(r_n, \theta_n) \} \\ (\tfrac{\partial^2}{\partial y^2} + k_0^2) I_n(x,y) = \; & \Delta X_n \Delta Y_n k_0^2 \{ H_0^{(1)}(k_0 r_n)\cos^2\theta_n + \tfrac{H_1^{(1)}(k_0 r_n)}{k_0 r_n}(\sin^2\theta_n - \cos^2\theta_n) \\ & \tfrac{\Delta X^2}{24}(\tfrac{\partial^2}{\partial y^2} + k_0^2) A(r_n, \theta_n) \tfrac{\Delta Y^2}{24}(\tfrac{\partial^2}{\partial y^2} + k_0^2) B(r_n, \theta_n) \} \end{aligned} \tag{A15}$$

where

$$\begin{aligned} \tfrac{\partial^2}{\partial x^2} A(r_n, \theta_n) = \; & k_0^2 \{ H_0^{(1)}(k_0 r_n)[\cos^2\theta_n(\tfrac{3}{8}\cos^2\theta_n + \tfrac{1}{8}\sin^2\theta_n) \\ & + \tfrac{2\sin^2\theta_n}{(k_0 r_n)^2}(3\cos^2\theta_n - \sin^2\theta_n)] \\ & + H_1^{(1)}(k_0 r_n^q)[\tfrac{5}{k_0 r_n^q}\cos^2\theta_n^q \sin^2\theta_n^q - \tfrac{4\sin^2\theta_n}{(k_0 r_n)^3}(3\cos^2\theta_n - \sin^2\theta_n)] \\ & + H_2^{(1)}(k_0 r_n)[-\tfrac{1}{2}\cos^4\theta_n + \tfrac{\sin^2\theta_n}{(k_0 r_n)^2}(-9\cos^2\theta_n + \sin^2\theta_n)] \\ & + H_4^{(1)}(k_0 r_n)[\tfrac{1}{8}\cos^2\theta_n(\cos^2\theta_n - \sin^2\theta_n)] \}, \end{aligned} \tag{A16}$$

$$\begin{aligned}\frac{\partial^2}{\partial z^2}A(r_n,\theta_n) = \; & k_0^2\{H_0^{(1)}(k_0r_n)[\sin^2\theta_n(\tfrac{3}{8}\cos^2\theta_n+\tfrac{1}{8}\sin^2\theta_n)\\ & +\tfrac{2\cos^2\theta_n}{(k_0r_n)^2}(\cos^2\theta_n-3\sin^2\theta_n)]\\ & +H_1^{(1)}(k_0r_n)[-\tfrac{4}{k_0r_n}\cos^2\theta_n\sin^2\theta_n+\tfrac{4\cos^2\theta_n}{(k_0r_n)^3}(3\sin^2\theta_n-\cos^2\theta_n)]\\ & +H_2^{(1)}(k_0r_n)[-\tfrac{1}{2}\sin^2\theta_n\cos^2\theta_n+\tfrac{\cos^2\theta_n}{(k_0r_n)^2}(9\sin^2\theta_n-\cos^2\theta_n)]\\ & +H_4^{(1)}(k_0r_n)[\tfrac{1}{8}\sin^2\theta_n(\cos^2\theta_n-\sin^2\theta_n)]\},\end{aligned} \tag{A17}$$

$$\begin{aligned}\frac{\partial^2}{\partial x^2}B(r_n,\theta_n) = \; & k_0^2\{H_0^{(1)}(k_0r_n)[\cos^2\theta_n(\tfrac{3}{8}\sin^2\theta_n+\tfrac{1}{8}\cos^2\theta_n)\\ & +\tfrac{2\sin^2\theta_n}{(k_0r_n)^2}(\sin^2\theta_n-3\cos^2\theta_n)]\\ & +H_1^{(1)}(k_0r_n)[\tfrac{\sin^2\theta_n}{k_0r_n}(-4\cos^2\theta_n+\sin^2\theta_n)+\tfrac{4\sin^2\theta_n}{(k_0r_n)^3}(3\cos^2\theta_n-\sin^2\theta_n)]\\ & +H_2^{(1)}(k_0r_n)[-\tfrac{1}{2}\sin^2\theta_n\cos^2\theta_n+\tfrac{\sin^2\theta_n}{(k_0r_n)^2}(9\cos^2\theta_n-\sin^2\theta_n)]\\ & +H_4^{(1)}(k_0r_n)[\tfrac{1}{8}\cos^2\theta_n(\sin^2\theta_n-\cos^2\theta_n)]\},\end{aligned} \tag{A18}$$

$$\begin{aligned}\frac{\partial^2}{\partial z^2}B(r_n,\theta_n) = \; & k_0^2\{H_0^{(1)}(k_0r_n)[\sin^2\theta_n(\tfrac{3}{8}\sin^2\theta_n+\tfrac{1}{8}\cos^2\theta_n)\\ & +\tfrac{2\cos^2\theta_n}{(k_0r_n)^2}(3\sin^2\theta_n-\cos^2\theta_n)]\\ & +H_1^{(1)}(k_0r_n)[\tfrac{5}{k_0r_n}\sin^2\theta_n\cos^2\theta_n-\tfrac{4\cos^2\theta_n}{(k_0r_n)^3}(3\sin^2\theta_n-\cos^2\theta_n)]\\ & +H_2^{(1)}(k_0r_n)[-\tfrac{1}{2}\sin^4\theta_n-\tfrac{\cos^2\theta_n}{(k_0r_n)^2}(9\sin^2\theta_n-\cos^2\theta_n)]\\ & +H_4^{(1)}(k_0r_n)[\tfrac{1}{8}\sin^2\theta_n(\sin^2\theta_n-\cos^2\theta_n)]\}.\end{aligned} \tag{A19}$$

We also note that an exact analytical expression for $\frac{\partial^2}{\partial x\partial y}I_n(x,y)$ can be obtained without using the Taylor expansion and is given by

$$\begin{aligned}\frac{\partial^2}{\partial x\partial y}I_n(x,y) = \; & H_0^{(1)}(k_0\sqrt{(x-x_n-\tfrac{\Delta X_n}{2})^2+(y-y_n-\tfrac{\Delta Y_n}{2})^2})\\ & -H_0^{(1)}(k_0\sqrt{(x-x_n-\tfrac{\Delta X_n}{2})^2+(y-y_n+\tfrac{\Delta Y_n}{2})^2})\\ & -H_0^{(1)}(k_0\sqrt{(x-x_n+\tfrac{\Delta X_n}{2})^2+(y-y_n-\tfrac{\Delta Y_n}{2})^2})+\\ & H_0^{(1)}(k_0\sqrt{(x-x_n+\tfrac{\Delta X_n}{2})^2+(y-y_n+\tfrac{\Delta Y_n}{2})^2})\end{aligned} \tag{A20}$$

When the observation point is in the center of the cell itself, the Taylor series expansion cannot be used. In this case we can employ the small argument expansion of the Hankel function, i.e.

$$H_0^{(1)}(x) \approx (1 - \frac{x^2}{4}) + \frac{2i}{\pi}[(\ln\frac{x}{2} + \gamma)(1 - \frac{x^2}{4}) + \frac{x^2}{4}]. \tag{A21}$$

Then at the center of the cell (self-cell contribution)

$$\begin{aligned} I_n(x_n, y_n) = \; & \tfrac{i4}{\pi}\{\tfrac{k_0^2 \Delta X_n \Delta Y_n}{2}[\gamma - \tfrac{i\pi+3}{2} + \ln(\tfrac{k_0\sqrt{(\Delta X_n)^2+(\Delta Y_n)^2}}{2})] \\ & +(\tfrac{k_0 \Delta X_n}{2})^2 \arctan(\tfrac{\Delta Y_n}{\Delta X_n}) + (\tfrac{k_0 \Delta Y_n}{2})^2(\tfrac{\pi}{2} - \arctan(\tfrac{\Delta Y_n}{\Delta X_n}))\}. \end{aligned} \tag{A22}$$

Using the same expansion we can also get

$$\begin{aligned} (\tfrac{\partial^2}{\partial x^2} + k_0^2) I_n(x_n, y_n) = \; & \tfrac{i4}{\pi}\{\tfrac{k_0^2 \Delta X_n \Delta Y_n}{4}[\gamma - \tfrac{i\pi+3}{2} + \ln(\tfrac{k_0\sqrt{(\Delta X_n)^2+(\Delta Y_n)^2}}{2})] \\ & +2\arctan(\tfrac{\Delta Y_n}{\Delta X_n}) + (\tfrac{k_0 \Delta Y_n}{2})^2(\tfrac{\pi}{2} - \arctan(\tfrac{\Delta Y_n}{\Delta X_n}))\}, \end{aligned} \tag{A23}$$

$$\begin{aligned} (\tfrac{\partial^2}{\partial y^2} + k_0^2) I_n(x_n, y_n) = \; & \tfrac{i4}{\pi}\{\tfrac{k_0^2 \Delta X_n \Delta Y_n}{4}[\gamma - \tfrac{i\pi+3}{2} + \ln(\tfrac{k_0\sqrt{(\Delta X_n)^2+(\Delta Y_n)^2}}{2})] \\ & +2(\tfrac{\pi}{2} - \arctan(\tfrac{\Delta Y_n}{\Delta X_n})) + (\tfrac{k_0 \Delta X_n}{2})^2 \arctan(\tfrac{\Delta Y_n}{\Delta X_n})\}. \end{aligned} \tag{A24}$$

The evaluation of the second order derivatives of $I_n(x, y)$ (expressions in (A15)) gives accurate results when $r_n \geq \lambda/60$. For smaller values of r_n the small argument expression for the Hankel function can be used. In such cases we have

$$\begin{aligned} (\tfrac{\partial^2}{\partial x^2} + k_0^2) I_n(x, y) = \; & F_1(x, y) - F_2(x, y) \\ (\tfrac{\partial^2}{\partial y^2} + k_0^2) I_n(x, y) = \; & G_1(x, y) - G_2(x, y) \end{aligned} \tag{A25}$$

where

$$\begin{aligned} F_i(x, y) = \; & k_0^2 \tfrac{\Delta X_n}{2} b_{ni}(\tfrac{3i}{\pi} - \tfrac{2i\gamma}{\pi} - 1) + (\tan\tfrac{a_{n2}}{b_{ni}} - \tan\tfrac{a_{n1}}{b_{ni}})(\tfrac{2i}{\pi} - \tfrac{ik_0^2 b_{ni}}{\pi}) \\ & -\tfrac{ib_{ni}k_0^2}{\pi}[a_{n2}\ln\tfrac{\sqrt{a_{n2}^2+b_{ni}^2}}{2} - a_{n1}\ln\tfrac{\sqrt{a_{n1}^2+b_{ni}^2}}{2}] \\ G_i(x, y) = \; & k_0^2 \tfrac{\Delta Y_n}{2} a_{ni}(\tfrac{3i}{\pi} - \tfrac{2i\gamma}{\pi} - 1) + (\tan\tfrac{b_{n2}}{a_{ni}} - \tan\tfrac{b_{n1}}{a_{ni}})(\tfrac{2i}{\pi} - \tfrac{ik_0^2 a_{ni}}{\pi}) \\ & -\tfrac{ia_{ni}k_0^2}{\pi}[b_{n2}\ln\tfrac{\sqrt{b_{n2}^2+a_{ni}^2}}{2} - b_{n1}\ln\tfrac{\sqrt{b_{n1}^2+a_{ni}^2}}{2}] \end{aligned} \tag{A26}$$

with

$$a_{ni} = \begin{cases} x - x_n - \frac{\Delta X_n}{2} & i = 1 \\ x - x_n + \frac{\Delta X_n}{2} & i = 2 \end{cases} \tag{A27}$$

$$b_{ni} = \begin{cases} y - y_n - \frac{\Delta Y_n}{2} & i = 1 \\ y - y_n + \frac{\Delta Y_n}{2} & i = 2 \end{cases} \tag{A28}$$

Now we are in a position to express the impedance matrix elements in terms of $I_n(x, y)$. The off-diagonal entries of the impedance matrix for the TM case are given by

$$Z_{mn}^{TM} = \frac{ik_0^2}{4}[\epsilon_r(x_m, y_m) - 1]I_n(x_m, y_m) \tag{A29}$$

and the diagonal entries are

$$Z_{nn}^{TM} = \frac{ik_0^2}{4}[\epsilon_r(x_n, y_n) - 1]I_n(x_n, y_n) - 1 \tag{A30}$$

For TE polarization, where the impedance matrix is composed of four sub-impedance matrices, the off-diagonal elements of each matrix are

$$\begin{aligned} Z_{1mn}^{TE} &= \tfrac{i}{4}[\epsilon_r(x_m, y_m) - 1][(\tfrac{\partial^2}{\partial x^2} + k_0^2)I_n(x_m, y_m)] \\ Z_{2mn}^{TE} &= \tfrac{i}{4}[\epsilon_r(x_m, y_m) - 1][\tfrac{\partial^2}{\partial x \partial y} I_n(x_m, y_m)] \\ Z_{3mn}^{TE} &= Z_{2mn}^{TE} \\ Z_{4mn}^{TE} &= \tfrac{i}{4}[\epsilon_r(x_m, y_m) - 1][(\tfrac{\partial^2}{\partial y^2} + k_0^2)I_n(x_m, y_m)] \end{aligned} \tag{A31}$$

and the diagonal elements are given by

$$\begin{aligned} Z_{1nn}^{TE} &= \tfrac{i}{4}[\epsilon_r(x_n, y_n) - 1][(\tfrac{\partial^2}{\partial x^2} + k_0^2)I_n(x_n, y_n)] - 1 \\ Z_{2nn}^{TE} &= 0 \\ Z_{3nn}^{TE} &= 0 \\ Z_{4nn}^{TE} &= \tfrac{i}{4}[\epsilon_r(x_n, y_n) - 1][(\tfrac{\partial^2}{\partial y^2} + k_0^2)I_n(x_n, y_n)] - 1 \end{aligned} \tag{A32}$$

The excitation vector elements for the TM and TE cases, respectively, are given by

$$e_m^{TM} = ik_0 Y_0[\epsilon_r(x_m, y_m) - 1]E_z^i(x_m, y_m), \tag{A33}$$

and

$$e_m^{TE} = ik_0 Y_0[\epsilon_r(x_m, y_m) - 1]E_x^i(x_m, y_m), \tag{A34}$$

$$e_{m+N}^{TE} = ik_0 Y_0[\epsilon_r(x_m, y_m) - 1]E_y^i(x_m, y_m). \tag{A35}$$

Once the matrix equation is solved for the polarization current, the scattered field can be computed at any point. The primary interest is the far field expressions which can be obtained by employing the large argument expansion of the Hankel functions. The scattered field, in far zone, is in the $\hat{z}$ and $\hat{\phi}$ directions for TM and TE polarization, respectively. If the polar coordinate of the scattering direction is denoted by (ρ, ϕ_s), in far zone we have

$$r_n \approx \rho - x_n \cos\phi_s - y_n \sin\phi_s \tag{A36}$$

and the far field amplitude for TM and TE are

$$\mathbf{P}^{TM} = \hat{z}\frac{-k_0 Z_0}{4}\sum_{n=1}^{N} J_z(x_n, z_n)\Delta X_n \Delta Y_n[1 - \frac{(k_0\Delta X_n)^2}{24}\cos^2\phi_s - \frac{(k_0\Delta Y_n)^2}{24}\sin^2\phi_s] \cdot e^{-ik_0(\cos\phi_s x_n + \sin\phi_s y_n)}, \tag{A37}$$

$$\mathbf{P}^{TE} = \hat{\phi}\frac{k_0 Z_0}{4}\sum_{n=1}^{N} \Delta X_n \Delta Y_n[1 - \frac{(k_0\Delta X_n)^2}{24}\cos^2\phi_s - \frac{(k_0\Delta Y_n)^2}{24}\sin^2\phi_s] \cdot e^{-ik_0(\cos\phi_s x_n + \sin\phi_s y_n)}[J_y(x_n, z_n)\cos\phi_s - J_x(x_n, z_n)\sin\phi_s]. \tag{A38}$$

4 Extension to Three-Dimensional Scattering

In this Section we obtain a connection between two- and three-dimensional radar cross section of a cylinder of infinite and finite length. The finite cylinder is just a section of the infinite cylinder and if the length is large compared with the wavelength we can assume the polarization current is identical with that of the infinite cylinder.

If the observation point is in xy plane and its direction is denoted by $\hat{k}_s$, the scattered field in the far zone of the cylinder is

$$\mathbf{E}^s \approx \frac{e^{ik_0 r}}{k_0 r} \frac{-ik_0^2 Z_0}{4\pi} \int_{-l/2}^{l/2} \int_s \hat{k}_s \times \hat{k}_s \times \mathbf{J}(r') e^{-ik_0 \hat{k}_s \cdot r'} \mathrm{d}s' \mathrm{d}z'. \tag{A39}$$

But $\mathbf{J}$ is independent of the axial variable z and the z integration can be carried out, in which case the expression for the far field amplitude reduces to

$$\mathbf{S} = \frac{-ik_0^2 Z_0}{4\pi} l \int_s \hat{k}_s \times \hat{k}_s \times \mathbf{J}(\rho') e^{-ik_0 \hat{k}_s \cdot \rho'} \mathrm{d}s'. \tag{A40}$$

For an infinitely long cylinder the electric field in far zone is approximated by

$$\mathbf{E}^s \approx \sqrt{\frac{2}{\pi k_0 \rho}} e^{i(k_0 \rho - \pi/4)} \frac{k_0 Z_0}{4} \int_s \hat{k}_s \times \hat{k}_s \times \mathbf{J}(\rho') e^{-ik_0 \hat{k}_s \cdot \rho'} \mathrm{d}s'. \tag{A41}$$

which results in the two-dimensional far field amplitude

$$\mathbf{P} = \frac{k_0 Z_0}{4} \int_s \hat{k}_s \times \hat{k}_s \times \mathbf{J}(\rho') e^{-ik_0 \hat{k}_s \cdot \rho'} \mathrm{d}s'. \tag{A42}$$

Now a comparison of equations (A40) and (A42) shows that

$$\mathbf{S} = \frac{-2iL}{\lambda} \mathbf{P}, \tag{A43}$$

and the relationship of the Two- and three-dimensional radar cross section is:

$$\sigma_3 = \frac{2L^2}{\lambda} \sigma_2. \tag{A44}$$